

The 74 MHz System on the Very Large Array

N. E. Kassim, T. Joseph W. Lazio

*Naval Research Laboratory, Remote Sensing Division, Code 7213, Washington, DC
20375-5351*

Namir.Kassim@nrl.navy.mil

Joseph.Lazio@nrl.navy.mil

W. C. Erickson

*U. of Tasmania, School of Math. & Physics, G.P.O. Box 252-21, Hobart, Tasmania 7001,
Australia*

R. A. Perley

National Radio Astronomy Observatory, P.O. Box O, Socorro, NM 87801

rperley@nrao.edu

W. D. Cotton

National Radio Astronomy Observatory, 520 Edgemont Road, Charlottesville, VA 22903

bcotton@nrao.edu

E. W. Greisen

National Radio Astronomy Observatory, P.O. Box O, Socorro, NM 87801

egreisen@nrao.edu

A. S. Cohen, B. Hicks

*Naval Research Laboratory, Remote Sensing Division, Code 7213, Washington, DC
20375-5351*

Aaron.Cohen@nrl.navy.mil

Brian.Hicks@nrl.navy.mil

H. R. Schmitt

*Naval Research Laboratory, Remote Sensing Division, Code 7215, Washington, DC
20375-5351*

and

Interferometrics, Inc., 13454 Sunrise Valley Drive, Suite 240, Herndon, VA 20171

Henrique.Schmitt@nrl.navy.mil

and

D. Katz

U.S. Naval Academy, Physics 9C, Annapolis, MD21402-5026

dkatz@usna.edu

ABSTRACT

The Naval Research Laboratory and the National Radio Astronomy Observatory completed implementation of a low frequency capability on the Very Large Array at 73.8 MHz in 1998. This frequency band offers unprecedented sensitivity (~ 25 mJy beam $^{-1}$) and resolution for low-frequency observations. The longest baselines in the VLA itself provide 25" resolution; the system has recently been extended to the nearby Pie Town antenna of the Very Long Baseline Array, which provides resolutions as high as 12". This paper reviews the hardware, the calibration and imaging strategies of this relatively new system. Ionospheric phase fluctuations pose the major difficulty in calibrating the array, and they influence the choice of calibration strategy. Over restricted fields of view (e.g., when imaging a strong source) or at times of extremely quiescent ionospheric "weather" (when the ionospheric isoplanatic patch size is larger than the field of view), an *angle-invariant* calibration strategy can be used. In this approach a single phase correction is devised for each antenna, typically via self-calibration; this approach is similar to that used at higher frequencies. Over larger fields of view or at times of more normal ionospheric "weather" when the ionospheric isoplanatic patch size is smaller than the field of view, we adopt a *field-based* strategy in which the phase correction depends upon location within the field of view. In practice we have implemented this second calibration strategy by modeling the ionosphere above the array using Zernike polynomials. Images of 3C sources of moderate strength are provided as examples of routine, angle-invariant calibration and imaging. Flux density measurements of a sub-sample

of these sources with previously well determined low frequency spectra indicate that the 74 MHz flux scale at the Very Large Array is stable to a few percent, and that flux densities tied to the Baars et al. value of Cygnus A are reliable to at least 5 percent. We also present an example of a wide-field image, devoid of bright objects and containing hundreds of weaker sources, constructed from the field-based calibration. The paper also reviews other practical aspects of low frequency observations, in so far as they differ from those encountered at higher frequencies, including aspects of interference excision and wide-field imaging. We close with a summary of lessons the 74 MHz system offers as a model for new and developing low-frequency telescopes.

Subject headings: instrumentation: interferometers — techniques: high angular resolution — techniques: image processing — techniques: interferometric — astrometry

1. Introduction

Radio astronomy began with the discovery of celestial radio emission by K. Jansky at 20.5 MHz (Jansky 1935). Throughout the 1950s and 1960s, key discoveries and technological advances in radio astronomy—at low-frequencies ($\nu \lesssim 100$ MHz) in particular—helped form the basis of modern astronomy, including:

- The introduction of non-thermal processes as an astrophysical source of emission (Alfvén & Herlofson 1950; Kiepenheuer 1950; Shkolovsky 1952), motivated by early observations of the diffuse Galactic radio emission at 160 MHz (Reber 1940), though it took some time for the importance of non-thermal processes to be accepted widely;
- The discovery of pulsars through observations at 81 MHz (Hewish et al. 1968); and
- The development of aperture synthesis interferometry at 38 MHz (Ryle & Vonberg 1946; Ryle et al. 1950; Mills 1952; Ryle 1952). (See also the work by Pawsey et al. (1946) and McCready et al. (1947) using a “sea interferometer” at frequencies between 75 and 3000 MHz.)

By the late 1960s and early 1970s, however, interest turned to obtaining high-resolution images. Powerful centimeter-wavelength interferometers began to provide sub-arcminute angular resolution (or sub-arcsecond resolution in the case of the VLA by the late 1970s) with dynamic ranges of several hundred or better.

Even so, a number of low-frequency interferometers continued to be constructed, some with truly impressive collecting areas ($\gtrsim 10^5 \text{ m}^2$), including the UTR-2 (Braude et al. 1978), the Culgoora Radioheliograph, the Cambridge Synthesis Telescope, and the Clark Lake TPT Radio Telescope (Erickson et al. 1982). However, with the exception of the MERLIN (Thomasson 1986; Leahy, Muxlow & Stephens 1989) and GMRT 151 MHz systems (Swarup 1990) and for all telescopes operating below 100 MHz, the maximum baselines were relatively limited ($\lesssim 5 \text{ km}$). The corresponding angular resolution was relatively poor ($\gtrsim 10'$), and the resulting high confusion levels meant poor sensitivities ($\gtrsim 1 \text{ Jy}$). The primary constraint on baseline length were the phase distortions imposed by the Earth's ionosphere over the intrinsically wide fields of view and the lack of suitable algorithms to compensate for the distortions. On baselines longer than a few kilometers, ionospheric phase distortions are severe enough to cause decorrelation, making higher-resolution imaging difficult to impossible, especially at the lowest frequencies ($\leq 100 \text{ MHz}$).

This paucity of large aperture, high-sensitivity, synthesis instruments operating below 100 MHz has left this portion of the radio spectrum poorly explored. Yet, there are a variety of topics that could be addressed by a sensitive, high-angular-resolution, low-frequency telescope including:

- Continuum spectra over much larger frequency dynamic ranges for studies of shock acceleration and spectral aging in Galactic (supernova remnants) and extragalactic (radio galaxies and galaxy cluster relics) sources;
- Efficient detection of large numbers of steep spectrum sources, which can be imaged in some cases, including high-redshift radio galaxies, shocks driven by infalling matter in clusters of galaxies, and pulsars in the Milky Way and possibly in external galaxies;
- Probing the ionized interstellar medium (ISM) via measurements of radio-wave scattering and absorption, the distribution of low-density ionized gas toward nonthermal sources, and hydrogen and carbon recombination line observations of very high Rydberg state atoms;
- The large opacity of H II regions below 100 MHz can enable distance determinations to various foreground objects, in both the Galaxy and external galaxies, from which the three-dimensional distribution and spectrum of cosmic-ray emissivity can be determined as well as being used to measure their emission measures, temperatures, pressures, and ionization states
- Detection of coherent emission from sources such as the Sun, Jupiter, pulsars, and possibly radio bursts from nearby stars and extrasolar planets.

While earlier experience with MERLIN and the VLA (and more recently with the GMRT) demonstrated that large (> 5 km) interferometers could compensate for ionospheric effects below ~ 330 MHz, a prototype 74 MHz system was the first to demonstrate that self-calibration techniques can correct for the large ionospheric-induced phase errors below 100 MHz. The prototype 74 MHz system consisted of eight of the VLA's 28 antennas equipped with 74 MHz receivers, and Kassim et al. (1993) were able to produce images with sub-arcminute resolutions and sub-Jansky sensitivities, thereby demonstrating that these self-calibration techniques were able to correct for ionospheric phase errors on baselines at least as long as the longest VLA baselines (35 km) and, in principle, much longer. Because of the limited number of antennas, the prototype 74 MHz system had relatively poor u - v coverage, so only the strongest (≥ 500 Jy) sources, numbering a dozen or so, were imaged.

In 1998 January all 28 VLA antennas were equipped with 74 MHz antennas. This improved the capability of the instrument greatly, and it is now possible to detect hundreds of sources in single fields at high angular resolution and sensitivity. At the same time, a number of innovative procedures and software solutions have been developed to handle the data, some of which are significantly different than at centimeter wavelengths and others of which are applicable to, and new to, centimeter wavelengths. Figures 1 and 2 illustrate the levels of resolution and sensitivity now possible with this new system, improvements that are all the more impressive given that the relatively modest collecting area and low efficiency of the VLA ($\simeq 2 \times 10^3$ m² effective collecting area, $\lesssim 10\%$ of many of the other telescopes shown).

This paper describes the fully operational 74 MHz system (hardware and software) on the VLA. In §2 we summarize briefly the characteristics of the prototype array as they relate to the current system. In §3 we review general characteristics of the current low frequency system, summarize its general performance, and highlight those aspects that are significantly different than at centimeter wavelengths. We describe the calibration of 74 MHz observations in §4 and their imaging in §5. In §6 we suggest how the current system could be improved via dynamic scheduling. In §7 we discuss possible future expansions of low-frequency synthesis instruments using the lessons from the 74 MHz system, and we present our conclusions in §8. In Appendix A we present selected examples of imaging of moderately strong 3C sources.

Throughout the paper we shall illustrate various effects with images or other figures produced from 74 MHz observations. The examples we show are a heterogeneous lot, resulting from a number of different observations of different sources acquired for different purposes. Our objective is to present a representative sample of various effects, but not all effects will necessarily be present in every observation.

2. Low-Frequency Systems on the VLA

The original design of the Very Large Array included only four frequency bands, centered near wavelengths of 21, 6, 2, and 1.3 cm (Napier et al. 1983). However, there is no fundamental reason a low-frequency system cannot operate on the array—the principles of aperture synthesis are as applicable to 50 MHz as they are to 5 GHz. More importantly, the key components of the array—the signal collection (antennas), signal transmission (waveguide), and signal processing (correlator and post-processing)—are essentially frequency independent within the radio part of the spectrum. As soon as the construction phase of the VLA ended, discussions on implementing a low-frequency capability began.

Perley & Erickson (1984) advocated a free-standing array that would make use of the VLA’s infrastructure (most importantly, the waveguide transmission system) to achieve approximately 25" resolution. However, no source of funding was obvious, and it was decided subsequently that trial systems could be implemented on the VLA itself to address key questions regarding the calibration and imaging of low frequency, long-baseline data.

The initial low-frequency system, operating at 90 cm (300 to 340 MHz), was installed between 1983 and 1989. It is a prime-focus system, as it is impractical to implement a secondary focus system at such a low frequency. The feed is a crossed dipole, situated in front of the Cassegrain subreflector, which thus acts as a (rather imperfect) ground plane. Because of this, and because the phase center is located approximately 50 cm ($\approx \lambda/2$) in front of the true focus, this system has both a low efficiency (less than 40%) and a very broad shoulder of width approximately 12° in the antenna power pattern. Nevertheless, it has been a very successful and widely used frequency band at the VLA. Most importantly, it encouraged the development of the multi-faceted imaging algorithms (Cornwell & Perley 1992) needed for wide-field, low-frequency observing, as described later in this paper. Its operation also demonstrated the robustness of angle-independent self-calibration (§4.4) for removing ionospheric distortions across the large ($\sim 2.5^\circ$ FWHP) 90 cm field of view.

The success of the 330 MHz system soon led to consideration of a lower frequency facility. A protected radio astronomy frequency allocation exists between 73 and 74.6 MHz. Again, funding constraints led to the decision to deploy a trial system, comprising a simple feed system on a few of the VLA’s antennas.

The feed system chosen is essentially the same as that used at 330 MHz—crossed dipoles in front of the subreflector. Because of the long wavelength, the defocussing errors that affect 330 MHz performance severely are not serious at 74 MHz. However, because the antenna itself is only approximately 6λ in diameter, the subreflector is an imperfect ground plane, and the profound effect of the antenna quadrupod structure, it was anticipated that the

forward gain and sidelobe structure would be fairly poor—as subsequent measurements have borne out. Kassim et al. (1993) describe the prototype 74 MHz system in more detail and describe the initial data calibration and imaging methodologies.

3. The 74 MHz System on the VLA

Amplifiers and feeds for the complete 74 MHz system were built during the summer of 1997 by two of us (WCE and BH) at the NRL and deployed during the fall of that year. All antennas were equipped with dipoles by 1998 January.

Because of concerns about blockage at higher frequencies, a deployable crossed-dipole feed was designed. The half-wavelength dipoles contribute to blockage and a higher system temperature, resulting in a total sensitivity loss of about 6% at 1.4 GHz and smaller losses at higher frequencies, so they are deployed only during a fraction of the time in each configuration. A simple mounting system is used—two ropes, each of which supports one dipole, are threaded through eyebolts located on opposite quadrupod legs at the appropriate height. The ends of these ropes are tied to cleats located at a convenient height on the quadrupod legs. The signal cables drop about 7 m to the antenna surface, where they pass through the roof of the vertex room to the amplifiers. Figure 3 shows the dipoles and mounting system developed.

The receiver units combine the linearly polarized signals of the dipoles to produce circular polarized signals, then amplify and bandpass filter these signals, and pass them to the VLA intermediate frequency (IF) system. They also contain an integral noise calibration source. In order to produce serviceable receivers on a short timescale and at low cost, they were constructed almost entirely from commercial components.

The VLA signal transmission system allows for two pairs of two parallel-hand signals to be transmitted. The receiver system is designed so that the two senses of circular polarization from the 74 MHz receivers occupy one pair of signal transmission channels while the two senses of circular polarization at 330 MHz occupy the other pair of signal transmission channels. Thus, 74 and 330 MHz observations can be acquired simultaneously. Kassim et al. (1993) used this simultaneous, dual-frequency capability for ionospheric calibration via phase transfer from 330 to 74 MHz (see §4). An alternate signal transmission approach is to use one pair of signals for the upper half of the 1.5 MHz bandpass and the other pair for the lower half, thereby obtaining higher spectral resolution, primarily for radio frequency interference (RFI) excision purposes (§4.2). Measurements of circular polarization are normally available and have been used for both astronomical (solar, T. Bastian, private communication, 1998)

and RFI excision purposes.¹

Figure 4 presents a complete block diagram of a receiver. In detail, the receiver units are comprised of the following components:

1. The two orthogonal linear feeds are converted by a full quad hybrid into right and left circular polarizations (RCP, LCP).
2. An onboard source injects a noise calibration signal into both the RCP and LCP chains via directional couplers. This source is directly powered by a “Cal” signal provided by the site.
3. Out-of-band rejection filtering is provided by high-Q cavity filters with a center frequency of 73.9 MHz and a 1.7 MHz bandwidth. Such a narrow bandwidth is necessitated by the close proximity of local television stations. (Tests have been conducted with a 3 MHz bandwidth; the TV signals saturated the receivers.)
4. For the VLA, the signal is transferred directly to the IF system while for the PT receiver, the signal is upconverted in order to pass into the VLBA IF system, by mixing the RCP and LCP channels with a reference local oscillator (LO) signal.
5. Two power combiners consolidate the 74 and 330 MHz channels for transport to the correlator.

The initial work on the 74 MHz system focused on the VLA alone. Concurrently NRAO was in the process of testing fiber optic transmission techniques by tying in the nearby Pie Town antenna (PT) of the Very Long Baseline Array (VLBA). First fringes between a VLA subarray and the PT antenna were observed in 1998 December, and a successful test with the PT antenna and the full VLA was conducted in 1999 September. Routine observations on this facility began in 2000 October. Consequences of this fiber-optic link to Pie Town (the PT link) are that the longest VLA baselines are extended to approximately 70 km, but the number of antennas in the VLA decreases to 26 because the PT antenna replaces one of

¹VLA correlator modes ‘PA’ or ‘PB’ allow obtaining full polarization information at 74 MHz alone, at the expense of halving the number of channels, and thus reducing the ability to purge narrowband RFI. Tests observing a strong, unpolarized source indicate cross-polarization leakage of at least $\sim 30\%$, and since initial attempts at polarization calibration using AIPS task POLCAL failed, users have not been encouraged to utilize this mode. It is possible that a dedicated effort with the EVLA correlator might permit full polarization astronomical measurements in the future, although it is suspected that many, except relatively nearby sources, might be depolarized at this frequency due to Faraday rotation.

the antennas in the VLA and the VLA signal electronics requires removing another antenna from the array to accommodate the PT signal.

Initial efforts on the PT link focused on frequencies above 1000 MHz. The VLBA does have a standard observing frequency at 330 MHz, but it does not have a 74 MHz operating capability. In 2000, NRL and NRAO initiated a program to add a 74 MHz capability to the PT antenna and to operate the PT link at both 74 and 330 MHz. Initial tests were conducted with the 74 MHz receiver replacing the 330 MHz receiver, but the electronics path has been modified subsequently to operate at both 74 and 330 MHz simultaneously. Figure 5 shows the first successful fringes at 74 MHz, obtained on the quasar 3C 123 in the fall of 2001. In the remainder of this paper we shall focus on the VLA system alone. Many of the techniques we describe are equally applicable to observations with the PT link, though experience with that system is considerably more limited and has only been used to observe relatively bright, isolated objects (Gizani et al. 2005; Lazio et al. 2006; Lane et al. 2006; Delaney et al. 2004). See Appendix A for an example of the full synthesis VLA+PT image of Cas A (Figure 21).

Table 1 summarizes the performance characteristics of the VLA’s 74 MHz system. We quote a sky-noise dominated system temperature that is appropriate for the Galactic polar caps. While the sky-noise for fields on the Galactic plane can be up to ten times higher, in practice the low forward gain of the primary beam smooths out and lowers the variations in T_{sys} to typically a factor of two or less (§4.3) The sensitivity listed is typical for the A and B configurations, for regions away from the Galactic plane. Sensitivities for the smaller configurations are considerably poorer, because of confusion (§5.1) and presumably because of low-level, broad-band RFI from the antennas and equipment located at the VLA site.

Figure 6 shows the primary beam power pattern measured for one of the antennas. Other antennas show similar power patterns. Table 1 cites the primary beamwidth as $11^\circ.7$, but it is clear that the beam has only a modest forward gain and a broad plateau with a poor sidelobe structure. These result from the aforementioned aspects of the system that the antenna itself is only approximately 6λ in diameter and the antenna quadrupod structure. Notice that the sharp edge seen on the right side of the beams presented in Figure 6 is due to the fact that this portion of the beam was not sampled. This was due to motion limitations of the VLA antennas during the holography measurements used to determine the beam power pattern. Nevertheless, this sampling issue did not affect the mapping of the most important part of the beam, down to 20-25 dB from the peak. The poor primary beam definition gives rise to significant sidelobe confusion, as discussed below and further in §5.1.

Figures 7 and 8 show the system sensitivity, as measured by the rms noise level in an image, as a function of increasing receiver bandwidth and integration time. This behaviour is typical of observations obtained in the A and B configurations. These images were excised of

narrow-band RFI, calibrated and imaged following the procedures described in Sections 4 and 5. The deviation from a $\Delta\nu^{-1/2}$ dependence with increasing receiver bandwidth in Figure 7 indicates that the system is not thermal noise limited. On the other hand, Figure 8 shows an approximate $t^{-1/2}$ dependence normally indicative of a thermal noise limited response. Taken together we conclude that we are mainly sidelobe confusion limited since its effects should be independent of bandwidth to first order, but scale roughly as $t^{-1/2}$ because sources moving through the sidelobes contribute noise in a random walk fashion that averages out with time ² For integrations of ≥ 1 hr, the deviation from thermal noise is typically a factor of 2-4.

The residual effects of incompletely removed RFI must also play a role in the reduced sensitivity. In fact the sensitivity in the C and D configurations is much poorer than expected from confusion alone, and our hypothesis is that the effects of low-level, broad-band RFI are responsible for that. In practice the 74 MHz system is rarely used in either the C or D configurations.

We note that while Table 1 quotes an 8 hour sensitivity limit of 25 mJy, in practice the achievable sensitivity may vary considerably due to the positionally dependent sky noise dominated system temperature, and more importantly from the relative proximity to the handful of extremely bright sources that often dominate the sidelobe confusion (e.g. Cyg A, Cas A, etc.) In §5.1 we discuss both sidelobe and classical confusion further, and show that in the more compact configurations the latter effect can become significant.

4. Calibration of 74 MHz VLA Data

Observations of the brightest sources in the sky (e.g., Cyg A, Tau A) with the prototype 74 MHz system demonstrated that the methodologies and algorithms that had been developed for calibration at the standard VLA frequencies were generally sufficient for 74 MHz (Kassim et al. 1993), with self-calibration being particularly important. The larger number of antennas now available makes self-calibration even more robust, but it has also revealed its limits more clearly.

In this section we motivate and describe the procedures we have developed for the calibration and imaging of 74 MHz data. The procedure can be summarized as follows:

²One might expect this dependence to disappear once the u - v coverage repeats. In practice, however, position shifts caused by the ionosphere (§4.5) act to “thermalize” the sidelobe confusion contribution. Thus, we believe that the noise due to sidelobe confusion will continue to decrease, at least initially, as $t^{-1/2}$ even after the u - v coverage repeats.

Bandpass calibration (§4.1) Observations at 74 MHz are acquired in a spectral line mode, both to enable RFI excision and to avoid bandwidth smearing over the relatively large fields of view. Therefore we need to apply a baseline correction to the data.

RFI excision (§4.2) Largely because of self-interference, 74 MHz data always must be edited to remove RFI.

Amplitude calibration (§4.3) As at higher frequencies, a source whose flux density is presumed to be known must be observed to set the flux density scale. The primary flux density calibrator for the VLA at 74 MHz is Cyg A. Other sources that can be used when Cyg A is not available are Cas A, Vir A, 3C 123 and Tau A.

Phase calibration The dominant source of phase corruption at low frequencies is due to the Earth’s ionosphere. Unlike at higher frequencies, one cannot employ as a phase calibrator a source nearby in the sky to one’s target source or field. Instead we have developed two strategies:

- When the isoplanatic patch (scale over which the rms phase difference between two lines of sight is approximately 1 radian) size is larger than the field of view of interest (§4.4), a single phase calibration can be applied to the entire field of view. It is most useful in the more compact configurations (C and D) or in the larger configurations (A and B) when imaging a strong source. This strategy relies heavily on current implementations of self-calibration, and it is similar to the calibration strategy used by Kassim et al. (1993). As such, this strategy is a confirmation of their prediction that self-calibration can be used to remove ionospheric phase fluctuations.
- When the isoplanatic patch size is smaller than the field of view of interest (§4.5), an angular dependence *within the field of view* of interest must be used in the phase calibration. We have used a method called “field-based” calibration to do this, which models the ionosphere as a phase-delay screen and uses a grid of background sources to solve for the ionospheric refraction, both globally and differentially within the field of view.

Following sections describe imaging requirements (§5) and present examples designed to illustrate the efficacy of both phase calibration strategies (§A). This section parallels closely the discussion in our online tutorial³, which contains more detailed descriptions of the procedures, as well as sample inputs for reducing data within AIPS.

³<http://rsd-www.nrl.navy.mil/7210/7213/LWA/tutorial>

4.1. Bandpass Calibration

As described below (§4.2), the VLA generates considerable internal radio frequency interference. Consequently, observations are performed in a spectral-line mode, which also avoids bandwidth smearing over the large regions (typically) imaged (§5). Characteristic spectral channel bandwidths are 12 kHz in a 1.5 MHz total bandpass. As with any spectral line observation, the amplitude variations across the band (and phase gradients due to delay errors) must be removed by bandpass calibration. Fortunately, the flux density of Cyg A ($\simeq 17$ kJy) is nearly always much greater than the equivalent flux density of any RFI, even in the narrowest channels that the VLA correlator can produce (12 kHz), meaning that one can use observations of it to calibrate the bandpass prior to excising RFI. Other sources—such as Cas A, Vir A, Tau A—can also be used; their lower signal-to-noise ratios on longer baselines can require judicious choices of time or frequency ranges or both in order to calibrate the bandpass.

Bandpass calibration is traditionally performed with the assumption that the flux density of the calibrator can be represented by a single value across the bandpass. In the case of 74 MHz observations with the VLA, however, the fractional bandwidth of the system is large enough that the intrinsic visibility of Cyg A can change across it. A rough estimate shows that the effect of resolution can be ignored if

$$\pi \frac{\Delta\nu}{\nu} \frac{\theta_{\text{src}}}{\theta_{\text{HPBW}}} \ll 1, \quad (1)$$

where $\Delta\nu/\nu$ is the fractional bandwidth and $\theta_{\text{src}}/\theta_{\text{HPBW}}$ is the source size expressed in units of the synthesized beam. In the A configuration, the left-hand side of equation (1) is 0.3, so there is a 30% change (worst case) in visibility across the bandpass on the longest baseline; in the smaller configurations, the error introduced by the fractional bandwidth is proportionally less.

Two options exist for dealing with the effects of the intrinsic visibility change across the bandpass. First, one can set an upper limit to the baseline length to be considered, effectively decreasing $\theta_{\text{src}}/\theta_{\text{HPBW}}$. Second, one can divide the observed visibilities at each frequency by a model of the source, thereby transforming the visibilities into what would have been obtained had a point source been observed. In practice, the second option is used most often in order to employ the maximum amount of the data possible, and models⁴ of Cyg A, Cas A, Vir A, 3C 123 and Tau A are available online.

This second method, dividing the visibilities by a model of the source, is done before the

⁴<http://rsd-www.nrl.navy.mil/7210/7213/LWA/tutorial/>

visibility amplitudes are calibrated. At higher frequencies, the standard bandpass calibration procedure at the VLA is to divide by the “Channel 0” continuum data, formed by averaging the inner 75% of the bandpass. Rather than using a “Channel 0” continuum, which would be contaminated by the presence of the 100 kHz comb (§4.2), one first solves for the individual channel corrections (both amplitude and phase). These corrections are then normalized so that the mean correction across the spectrum is unity. Various weighting schemes can be used during the normalization process. In practice, the weights used in normalization are often taken to be independent of channel; the converse, scaling the weights by some function of the amplitude in each channel, can have the effect of giving more weight to baselines with more RFI (higher amplitudes) and the short baselines (which are most often affected by RFI).

In general a single bandpass correction is determined from all observations of the bandpass calibrator, and this correction is applied to all other observations within that “observing run.” For bright sources, residual bandpass calibration errors can introduce systematic errors in the image (appearing in the shape of the beam, but which cannot be CLEANed) and thereby limit the dynamic range of the image. In these cases, one of two strategies can be adopted. If one has multiple observations of the bandpass calibrator, one can attempt to form the bandpass correction as a function of time. Alternately, during self-calibration one can produce a different phase correction for each channel (or small number of channels).

4.2. RFI Excision

Radio frequency interference (RFI) is a significant problem for low frequency VLA observations, though we note that there is little *external* RFI within the passband of 73.0–74.6 MHz. RFI is the major limiting factor for the dynamic range of the data observed with the more compact VLA configurations (C and D), due to the interference between the individual antennas of the array. It also constitutes an important issue for the more extended configurations (A and B), and needs to be dealt with appropriately. Essentially all non-astronomical signals are generated internally by the electronics of the VLA’s antennas and (to a lesser degree) signals emanating from other sources on the VLA site. By far the most common is a 100 kHz “comb” generated by the VLA’s monitor and control system. The oscillators responsible for this are located in every antenna. The oscillators can be coherent, with low phase rates such that phase differentials of less than 1 radian are obtained in an integration time, so that the coherence is maintained over long periods of time. The result is spurious correlation, especially between certain pairs of antennas whose oscillators appear to maintain coherence regardless of where they are located in the array. The net (averaged

over frequency) spurious visibility is not great ($\lesssim 100$ Jy) and can be effectively removed in the spectral domain. (By contrast, RFI at 330 MHz is mainly externally generated but can be excised using the same procedures as described below.) Figure 9 (left panel) shows an example of the 100 kHz “comb” for a single baseline.

Various procedures exist to accomplish RFI excision, depending upon the dynamic range requirements. Notice that the final image dynamic range will also depend on the position of the source in the field, usually being lower closer to brighter sources, and how well ionospheric effects can be solved (Sections 4.4 and 4.5). RFI excision appropriate for moderate dynamic range images ($DR \sim 10^3$) can be accomplished with the following procedure.⁵ One begins by identifying a “baseline” region within the spectrum to which only the astronomical source(s) and the noise within the system (i.e., T_{sys}) contribute. Usually, this “baseline” region is non-contiguous and does not include the “comb.” Next, visibilities with excessive amplitudes (e.g., 100σ) are flagged, regardless of where they appear in the spectrum (inside the baseline region or not). A linear fit to the “baseline” region is made and subtracted. The objective of this linear fit is to avoid (or reduce) the extent to which the flagging is biased by the astronomical source(s) and the system. Finally, visibilities whose residual values exceed a user-defined threshold (typically $6\text{--}8\sigma$) are flagged in channels both inside and outside of the “baseline” region. The results of this procedure are presented in the right panel of Figure 9, where we show the example of the visibility spectrum on a baseline after RFI editing. An inspection of this image shows that this procedure has eliminated the RFI emission present in the left panel.

A similar procedure, also appropriate for moderate dynamic range imaging, is to flag all of the channels comprising the 100 kHz comb⁶ and then clip any remaining data with excessively large amplitudes.

While elementary, these approaches have proven to be reasonably effective in removing RFI at 74 (and 330) MHz. Additional tests also have been found to be useful. For instance, channels in which the ratio of the real part of the visibility to the imaginary part exceeds a given value can be flagged. Various observers have noted that RFI can often be strongly circularly polarized so a test on the amplitude of the circular polarization (Stokes V parameter) in each channel is also useful. For the highest dynamic range images ($DR \sim 10^4$), it is often necessary to inspect the data by hand and perform additional editing.⁷ Lane et al.

⁵Within AIPS, this procedure is implemented using `FLGIT` or by `VLA FM`, a special-purpose task added to AIPS.

⁶Within AIPS, the task `SPFLG` can be used.

⁷ Within AIPS, the tasks `SPFLG`, `TVFLG`, and `WIPER` can be used either singly or in combination.

(2005) describe in more detail post correlation RFI excision with the VLA and VLBA (see also Golap et al. (2006)).

The limited spectral resolution of the VLA’s original correlator means that even the narrowest channels provided are 12 kHz wide. As a result, the procedure we describe can remove a significant fraction of the data—typically 10 to 25%. A key design goal of any future correlator would be to provide considerably more channels with higher frequency resolution, allowing much more precise removal of these artificial signals. Such improvements are forthcoming for the 74 MHz system with the transition to the EVLA and its WIDAR correlator. Furthermore, techniques of pre-correlation RFI excision would clearly offer key advances over current approaches.

A final note is that the discussion above focuses on narrow-band RFI, much of whose source is relatively well understood. Since the sensitivity and dynamic range in the rarely used C and D configurations appears worse than attributable to confusion or poorly excised narrow-band RFI, we hypothesize that an additional form of low-level, broad-band RFI is limiting the system performance in those configurations. That suggests that the source of interference is the VLA itself, or equipment at the site. Clearly another lesson for future instruments is design them with a focus on eliminating or at least shielding against self-generated RFI.

4.3. Amplitude Calibration

4.3.1. *Low-Frequency Calibration Problems and Advantages of the VLA System*

Despite relatively limited sensitivity compared to that typical of higher frequency observations, the sensitivity of the 74 MHz VLA is unprecedented for frequencies below 100 MHz, and so it has now become possible to obtain flux density measurements for thousands of radio sources that have never been measured before at these frequencies. However, it is important to note that flux density scales are rather uncertain below 100 MHz for several reasons.

First, the Galactic background dominates system noise temperatures, so system temperatures vary as an antenna is scanned across the sky and system gain and temperature must be measured continuously. Antenna gains vary at less than the few % level as a function of time and are consistent with elevation dependent deformation of the feed or dish structure being negligible at 4-m wavelength. This trend is consistent with elevation-dependent gain variations at L-band (20-cm) measured at less than 1%, while variations at P band (90-cm) have never been seen. T_{sys} certainly changes with time, as it depends on T_{sky} which is a strong

function of sky position, being much greater on the Galactic plane than off. Early single antenna tests showed variations of up to a factor of 2 between “on” and “off” regions against the Galactic plane - being greatest towards the Galactic center. This is much less than the known contrast in brightness temperature between inner regions of the Galaxy and cooler parts of the extragalactic sky as determined by early, lower resolution measurements (e.g. Yates 1968). However that real variation is diluted by the poor directivity of the 25-m dishes at 74 MHz, with $\leq 20\%$ of the power in the main beam and the rest scattered in sidelobes across the sky. Hence while T_{sys} does change as a function of time, the variation is greatly smoothed out and is normally less than a factor of two over the course of any pointed, full synthesis observations. A related consideration is that calibrator observations of calibrators like Cyg A not drive the system response into a regime in which a non-linear correction of its correlation coefficient is required. Fortunately the increase on T_{sys} when observing Cyg A is modest. A rough estimate from existing low resolution sky maps suggests an increase in T_{sys} of $\leq 40\%$ in the main beam alone, again consistent with early single antenna tests. Thus the contribution from the distributed “hot sky” still dominates the measured power, and are consistent with the measurements described below indicating that variations in system gain and temperature are being tracked accurately (see also Sections 3 and 5.1).

Second, many systems utilize fixed antennas whose power patterns are not very well determined. The relative flux densities of sources at adjacent declinations can be determined reliably because they traverse the same parts of the fixed antenna’s pattern, but measurements of sources at widely separated declinations are difficult. Also, many measurements must be made far from the maxima of the primary response patterns of the antennas, where the patterns are less stable than at the maxima. Finally, ionospheric amplitude scintillations often disturb measurements below 50 MHz and ionospheric absorption can affect them below 20 MHz.

The VLA has features that avoid most of these problems. First, the gain and noise temperature of each antenna are monitored continuously by the injection of noise calibration signals into every preamplifier. At higher frequencies, experience has shown that the gain properties of the VLA electronics system are stable at the 0.1% level, and that linearity is preserved even if the T_{sys} changes by a factor of 3 or more. Second, the VLA antennas are pointed at each source under observation, and the antenna power pattern is stable, at least for measurements made near its center. Sources at different declinations should be directly comparable. Third, 74 MHz is a high enough frequency that ionospheric amplitude scintillations and absorption are minimal, though occasional episodes of scintillations have been seen during observations of strong sources.

4.3.2. *VLA Calibration Method*

Because of the high system temperature of the 74 MHz system, the best source to use for calibrating the visibility amplitudes is Cyg A. However, as it is partially resolved, a good model is required for accurate amplitude and phase calibration. We have used multiple observations in multiple VLA configurations to generate such a model, and it is available online⁸. We base our flux density scale on that of Baars et al. (1977), in which Cyg A has a flux density of 17 086 Jy at 74 MHz. Although Cyg A is by far the best amplitude calibrator, other sources can be employed, if necessary. Vir A is acceptable in all VLA configurations, while Tau A and Cas A can be used in the smaller configurations. As with Cyg A, all of these sources are resolved significantly, so model images (available online) are necessary for calibration. The amplitude calibration is done in the usual way in AIPS, with the task CALIB used to derive the antenna complex gains. Residual amplitude errors are corrected by self calibration in the final stages of the reduction. As described below, measurements demonstrate that reliable fluxes, at the 5% level, can be obtained down to the half power beam point. In the rare case of severe ionospheric weather conditions such as ionospheric scintillations (§4.5.1), amplitude correction is not possible and the data are discarded.

4.3.3. *Reliability of the VLA flux-scale at 74 MHz*

In order to quantify our ability to cope in practice with the problems described above (§4.3.1), it is necessary to examine the robustness of the flux density scale for the VLA. As part of a snapshot survey (§A), we observed a number of strong sources, which we have used to constrain the gain stability of the 74 MHz system.

Kühr et al. (1981) presented the spectra of 518 extragalactic radio sources that have flux densities above 1 Jy at 5 GHz, using data compiled from many catalogs. The absolute flux density scale was based on that of Baars et al. (1977). Although the data below 100 MHz are rather sparse, the spectra of Kühr et al. (1981) have proven to be quite reliable in most cases. They do not include any sources near the Galactic plane and give analytic expressions for spectra only when they are fairly simple (straight or moderately curved). Sources with complex spectra are included in the catalog, but no attempt was made to fit such spectra with analytic expressions.

Of the 29 sources in our snapshot survey, eleven have spectra for which Kühr et al. (1981) give analytic expressions. Table 2 compares our measured 74 MHz flux densities with

⁸<http://rsd-www.nrl.navy.mil/7210/7213/lazio/tutorial/>

the value predicted at 73.8 MHz from those expressions. (See also Table 8.)

Because of their relatively simple structure even at the highest angular resolution, the four most reliable sources for comparison appear to be 3C 98, 3C 123, 3C 219, and 3C 274. These yield an average flux density ratio (VLA/Kühr et al. 1981) of 0.99 ± 0.06 . A simple average of all eleven ratios yields 0.98 ± 0.13 . In either case the agreement between the Kühr et al. (1981) and VLA flux density scales appears to be as good as 2%. We conclude that 74 MHz flux density measurements are stable at the few percent level, and that the absolute flux density scale as tied to the Baars et al. (1977) value for Cygnus A is accurate to at least 5%. These results also confirm that antenna system temperatures and gains are being tracked correctly, and that power is being detected linearly. Hence the 74 MHz flux scale is reliable for those sources never observed before at this frequency. However, Kühr et al. (1981) give correction factors that should be used to adjust the data from the various catalogs to their flux density scale. When making comparisons, these corrections should be used.

4.4. Angle-Independent Phase Calibration

The phase calibration procedure employed commonly at centimeter wavelengths makes use of a secondary calibrator, a modestly strong source much closer in the sky to the target source than the amplitude calibrator. It is chosen to be strong enough to dominate the total flux within its field of view, so that a unique phase can be derived for the contribution of the array’s electronics.

In contrast, at 74 MHz the field of view is so large that few sources are strong enough to dominate the field. Thus, an *initial* phase calibration is determined from Cyg A (or another strong source such as those listed above, §4.3), which usually provides sufficient coherence on enough short (≤ 10 km) baselines to form an initial image even if the target source is in a completely different portion of the sky. Oftentimes, coherence is retained even after the phases are smoothed over long time scales, even longer than the duration of the observation.

This technique works only for bright sources. Implicit in this procedure is the assumption that a single phase suffices for the entire field of view—hence its angle-invariant designation.

This initial phase calibration works because relatively larger scales ($\gtrsim 50$ km, i.e., larger than the VLA) present in the ionosphere dominate the phase fluctuations. It is also the reason previous low frequency (< 100 MHz) systems with baselines less than about 5 km were able to function without ionospheric correction techniques—except for a constant refractive shift arising from the large-scale structures, short baselines ($\lesssim 5$ km) were, to first order,

relatively unaffected by the ionosphere (Erickson 1984)⁹. The initial image obtained from this calibration must be subsequently astrometrically corrected and self-calibrated.

We write the observed phase on a given baseline as

$$\phi(t) = \phi_{\text{src}}(t) + \phi_{\text{VLA}} + \phi_{\text{ion}}(t) \quad (2)$$

where ϕ_{src} is the phase contributed by the intrinsic structure of the source, ϕ_{VLA} is the phase contributed by the VLA electronics, and ϕ_{ion} is the ionospheric contribution. We write $\phi(t)$ to emphasize that the phase is a function of time, not only because the Earth-rotation synthesis means that the phase can change as the array samples different portions of the u - v plane (ϕ_{src}) but also because of the temporal variations imposed by the ionosphere (ϕ_{ion}).¹⁰ During calibration observations of a strong source, the first term ϕ_{src} can be calculated and removed using a model of the source, so we shall ignore it henceforth.

The smallest scales in the ionosphere over which the rms phase varies by more than 1 radian at 74 MHz are typically no smaller than 5 km. As a result, the ionospheric phase term, ϕ_{ion} , can be considered to be relatively constant across at least the short baselines in the array ($\lesssim 5$ km). Transferring the phases determined toward the calibrator source (i.e., Cyg A) to another direction in the sky introduces a term, $\phi_{\text{ion,cal}}$, the ionospheric phase distortion toward the calibrator. However, for the short baselines, this term is effectively constant. It introduces little more than a refractive shift of the apparent source positions (Erickson 1984). This refractive shift can be removed by registering the image with an existing all-sky survey at a higher frequency (i.e., the NVSS, Condon et al. 1998; WENSS, Rengelink et al. 1997; and SUMSS, Bock et al. 1999).

This initial, crude phase calibration is sufficient to produce an image. The initial image then serves as the initial model for hybrid mapping, which consists of iterative loops between self-calibration and imaging. With the large number of antennas in the full VLA, convergence occurs rapidly. In this respect, the process is similar to that employed often in very long baseline interferometry (VLBI) in which a crude initial model is combined with several iterations of hybrid mapping to produce the final image (Walker 1995).

Phase self-calibration is warranted only if a sufficient signal-to-noise level can be ob-

⁹Short baselines are undoubtedly affected by small scale ionospheric structure beyond simple refractive shifts, but those effects were negligible for past arrays where the intrinsic sensitivity was already confusion limited to Jy-levels. As a new generation of low frequency arrays aims to achieve much greater levels of sensitivity, the phase variations due to small scale ionospheric structure may well be the limiting factor.

¹⁰In practice, ϕ_{VLA} can also be a function of time because of phase jumps in the electronics. These are sufficiently rare that we shall ignore them.

tained (Cornwell & Fomalont 1999). In practice there are two signal-to-noise level thresholds that must be met, but both can be exceeded quite easily. The first signal-to-noise threshold that must be met is that there must be a source or sources that are strong enough to be detected in the approximate ionospheric coherence time (≈ 1 min.). Both an extrapolation of higher frequency source counts (Bridle 1999) and source counts derived from 74 MHz observations indicate that there should be roughly 150 Jy of flux from different sources within the primary beam, originating from sources stronger than about 5 Jy, which is about 5 times the rms noise level obtained in a 1 min. integration time.

The second signal-to-noise threshold is that the phase derived from the calibrator source must dominate over weaker sources in the field. This criterion can be understood by considering the calibrator, with a flux density S_{cal} , to be immersed in a “sea” of randomly-located background sources, with a typical flux density S_b . Treating the visibilities of the sources as phasors, the background sources will contribute to a jitter of the phase determined for the calibrator. A rough estimate of the magnitude of this jitter is

$$\delta\phi \sim \sqrt{N} \frac{S_b}{S_{\text{cal}}}, \quad (3)$$

where N is the number of background sources in the field of view. For the purposes of a rough estimate, we take $\delta\phi \sim 0.2$ (implying a phase jitter signal-to-noise threshold of 5). With $S_b \sim 5$ Jy and $N \sim 40 (= 200 \text{ Jy}/5 \text{ Jy})$, we find $S_{\text{cal}} \sim 150$ Jy. Though clearly a rough estimate, experience has shown that it is possible to achieve successful phase self-calibration with as little as 50 Jy from bright sources in the initial model. More generally, nearly every randomly-picked field of view will contain at least one 3C object (or equivalent at southern declinations) whose flux density alone is close to this minimum value, and existing all-sky surveys at higher frequencies can be used to identify the (few) strongest objects totaling at least 100 Jy within the field of view. (The phase fluctuations in the top panel of Figure 5 are consistent with the estimate derived here for the phase jitter due to background sources.)

A potential weakness of this method is its limited utility to the larger configurations (A and B). Depending upon the state of the ionosphere, it may be difficult or impossible to obtain sufficient signal-to-noise on the more limited number of short baselines. In turn, this may impair one’s ability to produce an initial model for self-calibration.

An alternate phase calibration strategy does not rely on the phases transferred from a distant source. Instead, a strong source, like Cyg A, is used to establish the amplitude scale. An all-sky survey (particularly the NVSS or WENSS) is used to construct a sky model¹¹

¹¹Within AIPS, the sky model is constructed using FACES.

within the primary beam; for sources north of declination $+30^\circ$, the lower frequency WENSS is preferable to NVSS. This sky model then serves as an initial model for self-calibration. In effect, no attempt is made to use an external calibrator to calibrate the phases. A primary benefit of this approach is to produce a map with astrometrically correct positions, as the coordinate system of the map is locked to the *a priori* known position of sources in the sky, while self-calibration with a model produced from raw data locks the final position to an arbitrary sky position determined by the position of the model or ionospheric refraction. This alternate strategy is a simplified application of the field based phase calibration technique, described in the next section.

4.5. Field-Based Phase Calibration

The prior calibration strategy is most useful at 74 MHz within a restricted field of view containing a strong source or strong sources located relatively close together. In this section we first motivate why phase angle independent self-calibration is insufficient for all observations, then describe the method we have developed to handle more general observations.

4.5.1. Motivation

The isoplanatic patch is the characteristic scale over which the rms phase difference between two lines of sight is approximately 1 radian. At low frequencies the size of the isoplanatic patch is determined primarily by the ionosphere. The phase contributed by a cold plasma is

$$\begin{aligned}\phi &= r_e \lambda \int_0^D ds n_e(s), \\ &= r_e \lambda N_e,\end{aligned}\tag{4}$$

where r_e is the classical electron radius, λ is the free-space wavelength, n_e is the electron number density, and N_e is the electron column density (also known as the total electron column, TEC). For reference, two lines of sight for which $\Delta\phi \sim 1$ rad at 74 MHz would differ in electron column density (TEC) by $\Delta N_e \sim 10^{14} \text{ m}^{-2}$.

Two lines of sight separated by the diameter of the primary beam pierce the F-layer of the ionosphere (the most dense region of the ionosphere at an altitude of ~ 400 km) at a linear separation as large as 80 km. This is larger than the size of the array itself, even with the PT link, and the ionosphere can have significant column density variations at much smaller scales ($\lesssim 10$ km), so the primary beam typically includes multiple isoplanatic

patches. Figure 10, which itself is a portion of a larger image, shows the effect of constructing an image larger than the isoplanatic patch. Clearly evident is a systematic distortion of the sources attributable to incorrect phase calibration.

Figures 11–14 illustrate the successively higher order ionospheric effects that lead to the break-down of a simple angle-invariant self-calibration. Figures 11 and 12 shows the effects of the largest scale (> 1000 km) ionospheric structure, a “wedge” that acts to shift the entire field of view, without source distortion, on time scales of minutes. This structure dominates the total electron content (TEC) and also causes Faraday rotation of linear polarization. A GPS-based method to correct this effect has been demonstrated at the VLA (Erickson et al. 2001), but self-calibration alone can compensate for it if the time scale on which the phase corrections are calculated is sufficiently short to track this gross refraction. It will, however, leave the field with a gross astrometric offset from the correct source positions.

Figure 13 shows the phase effects imposed by ionospheric mesoscale structure. These mesoscale structures are due typically to traveling ionospheric disturbances (TIDs), with scale sizes on the order of hundreds of kilometers, column densities of order $10^{15.5}$ m^{-2} and periods less than 90 minutes. While the size of the VLA—even in its A configuration—is smaller than that of a TID, it is still sufficiently large that TIDs can impose a (mainly) linear phase gradient down the arms of the VLA. The effect of this linear phase gradient can be seen as a (nearly) linear increase in the phase with increasing distance from the array center; the amplitude of the offset also increases with baseline, as the antenna separation becomes a larger fraction of the TID. (In the example shown in Figure 13, the traveling nature of the disturbance is also present as a lag between the times when the maximum phase offset is obtained at the various antennas.) Self-calibration can remove the effects of TIDs only for a limited region in the field of view. At any given instant, sources outside this region are “differentially refracted” or shifted by varying amounts in proportion to their distance from nominal direction of the self-calibration solution. Because a typical observation lasts much longer than the time it takes a TID to pass over the array, the differential refraction changes with time. Thus, sources in a map made using all of the data are blurred as well.

Jacobson & Erickson (1992a,b) conducted an extensive study of acoustic gravity wave generated TIDs having phase speeds less than 200 m s^{-1} and periods greater than 10^3 s using the VLA at 330 MHz. They found them to have a quasi-isotropic distribution in azimuth. On shorter time scales (< 300 s) they found the ionospheric phase effects to be dominated by faster (> 200 m s^{-1}) magnetic eastward-directed disturbances (MEDs). Over the baseline relevant to the extended VLA configurations and the PT link (~ 50 km), both TIDs and MEDs contribute to 74 MHz phase effects.

Figure 14a-f were obtained from an 8 hour observation towards a strong source (Virgo

A), and illustrate a variety of effects due to ionospheric phenomena typically observed at the VLA on scales sizes both larger and smaller than TIDs. Figures 14 a and b illustrate first order effects on the visibility phase towards Virgo A. Figures 14 c and d track the flux density and apparent position of Virgo A, while Figures 14 e and f reflect differential refraction towards five field objects after the first order term has been removed. These differential phase effects due to smaller scale ionospheric structures, on scales of tens of kilometers, are the most intractable and pose A MAJOR challenge for future instruments. (The high frequency “jitter” superposed on the TID-produced structure in Figure 13 is also contribution from smaller scale structure.) These phase effects are generated by turbulent structures comparable to OR SMALLER than the size of the VLA, and lead to source distortion. There is no current means of correcting for these effects over a wide field of view and when they are severe, the data must be discarded. If these small-scale structures generate phase distortions larger than 1 radian on scales smaller than the size of the VLA antennas, the result is ionospheric scintillations (also illustrated in Figure 14). We believe that there will never be a means for compensating for this effect, at least so far as imaging applications are concerned, as the data are effectively smeared in phase before they arrive at the antennas. (Ionospheric scintillations can be useful for studying the ionosphere itself, though.) Fortunately ionospheric scintillations are rare at the VLA at 74 MHz, but when they do occur those portions of the data must be removed.

In principle, a data-adaptive calibration scheme, based on self-calibration, could be used to remove the phase errors that result from imaging a region larger than the isoplanatic patch. Current implementations of self-calibration¹² model the phase error on the i^{th} antenna at time t as a single quantity, $\delta\phi_i(t)$, equivalent to assuming that the isoplanatic patch has an infinite extent above the array. The key assumption for self-calibration—that errors can be modeled as being antenna-dependent—remains true for a data-adaptive scheme. Thus, a joint multi-source self-calibration, in which the calibration correction would become a function of position on the sky, $\delta\phi(t; \alpha, \delta)$, seems possible. Limited testing suggests that such a scheme could work, though it probably requires considerably better signal-to-noise than can be achieved with the VLA; no comprehensive attempt to implement and assess such a scheme has been performed yet. In principle such a technique might allow wide-field imaging across the full extent of the primary beam on the longest baselines allowed by natural limits of brightness temperature sensitivity (for a related discussion, see also Erickson (2006)).

When it is desired to image an entire field of view, the assumption of an infinite isopla-

¹²This description includes CALIB within AIPS.

natic patch is no longer valid. The effects of such an assumption can be seen as a tendency to detect a larger number of sources toward the direction of the strongest source in the field (Cohen et al. 2003). Figure 15 illustrates this effect in a field containing 3C 63 (≈ 35 Jy). The density of sources across the field is clearly non-uniform. Besides the effects of anisoplanaticity, which shows up at scales of $5\text{-}10^\circ$, the non-uniform density can also arise from two other related causes. First, if sufficiently high-order ionospheric distortions are present, they contribute to increasing phase errors at increasing distances from the effective phase center. Sources at large distances will be blurred, thereby decreasing their brightnesses. Second, Figure 16 demonstrates that the apparent source positions also wander over time. Because the amount and direction of the wander can vary both over the field of view and with time, sources are smeared further and their brightnesses decrease further. Only in the neighborhood of a strong source are the self-calibration solutions able to track the ionospheric phase distortions accurately. If one is interested in imaging only a strong source, the non-uniform distribution of sources is usually unimportant. If a field does not contain a strong source, the self-calibration solutions represent some “average” ionospheric phase distortion across the field. Again, depending upon the scientific problem being attacked, using angle-independent self-calibration may be sufficient.

4.5.2. Implementation

Compensation for higher order ionospheric phase distortions is required (Cotton & Condon 2002; Cotton et al. 2004), when the entire field of view is of interest (e.g., in the VLA Low-frequency Sky Survey Cohen et al. (2003, 2006)) or when the object of interest is “close” to a strong source.

The latter case happens fairly frequently given that the typical separation of 3C sources on the sky is approximately 8° , comparable to the size of the VLA field of view. Moreover, the dynamic range required to detect or image a weak source close to a strong source may impose much more stringent constraints on the need to determine the ionospheric phase than the approximate 1 radian criterion that we gave at the beginning of the previous section.

In such cases, we model the ionosphere as a phase-delay screen.¹³ We return to equation (2), assume that ϕ_{src} is calculable and can be removed, and expand the ionosphere term as

$$\phi = \phi_{\text{VLA}} + \phi_{\text{ion,lo}} + \phi_{\text{ion,hi}}. \quad (5)$$

¹³Within AIPS, this procedure is implemented using `VLAFM`, a special-purpose task added to AIPS.

Here $\phi_{\text{ion,lo}}$ refers to the phase distortion introduced by low spatial frequency structures in the ionosphere while $\phi_{\text{ion,hi}}$ refers to high spatial frequency structures. In order to make a division between “high” and “low” spatial frequencies (or “long” and “short” wavelengths) we make a “frozen-flow” approximation in which the ionospheric structures are assumed not to change internally over the time it takes for them to be transported across the array. Under this assumption, spatial and temporal scales become equivalent. The smallest structures ($\lesssim 10$ km) are transported at speeds of order 100 m s^{-1} on time scales of order 100 s. We consider these to be high spatial frequencies. Structures of 100 km or larger are transported across in time scales of order 15 min.; these are low spatial frequencies.

The large-scale structures are larger than even the maximum baselines of the A configuration. We therefore decompose the low-frequency ionosphere term into low-order Zernike polynomials

$$\phi_{\text{ion,lo}} = \sum_{n=1}^2 \sum_l A_n^l Z_n^l \quad (6)$$

where Z_n^l is the Zernike polynomial, A_n^l is the coefficient of that polynomial, and the standard conditions apply that $n \geq |l|$ and $n - |l|$ is even. The $n = 1$ terms account for the large-scale refractive shift of the field of view while the $n = 2$ terms describe astigmatism or differential refraction within the field of view. The $n = 0$ term is not used because it represents an overall phase advance or delay (“piston”) to which the interferometer is insensitive. We use Zernike polynomials because they represent a class of polynomials orthogonal on a circle. Thus, they are useful for representing distortions across the aperture of the array.¹⁴ Table 3 summarizes the polynomials used. The methodology is quite similar to that used in adaptive optics systems in optical astronomy. One important difference between our use of the Zernike polynomials and that in adaptive optics, however, is that these polynomials are used to describe wavefront errors in or near the aperture for the case of adaptive optics systems in optical astronomy whereas here they represent errors quite far from the aperture plane.

In order to derive the required corrections, snapshot images of sources in an “astrometric grid” are produced, and the offsets between the apparent and expected locations of sources in the astrometric grid are determined. The snapshots must be formed on short enough timescales so as to track the ionospheric phase variations, typically 1 min. or shorter. Both the NVSS and WENSS can be used to produce this astrometric grid as both are constructed at a high enough frequency and from a sufficiently large number of sources that the positions

¹⁴The phase-delay screen representation and Zernike modeling of the ionosphere is not strictly correct as the ionosphere is not in the far-field of the array. Nonetheless, we view the Zernike polynomials as a useful first step in modeling the ionosphere.

of sources within these catalogs is known to an accuracy much better than the synthesized beam at 74 MHz, even in the A configuration. From the source offsets, the coefficients of the Zernike polynomials can be found in a least-squares minimization. Figure 17 shows an example of a (subset) of an astrometric grid and the resulting $\phi_{\text{ion,lo}}$ over the VLA for a particular observation.

The snapshot images of the astrometric grid sources are useful only if two conditions are met. First, the ionosphere must be stable enough that sources are not defocused seriously but merely shifted from their expected positions by refraction. Second, one must be able to determine ϕ_{VLA} prior to forming the snapshot images. As in §4.4, the initial phase calibration is determined from observations of Cyg A, or another primary calibrator. For a single source at a well-known position, one need solve for only the $n = 1$ terms describing an overall refractive shift. Correcting for this global refractive shift should yield ϕ_{VLA} . If $\phi_{\text{ion,hi}}$ is non-negligible (meaning that sources may be defocused), it will corrupt estimates of ϕ_{VLA} . Because no phase calibration is performed during this strategy (but see below), any errors in determining ϕ_{VLA} remain in the data during all subsequent processing.

Figure 18 presents the same field as in Figure 15, only this time calibrated using this field-calibration strategy. The density of sources across the field is seen to be far more uniform. Figure 19 quantifies the improvement that the field-based calibration; it shows the rms jitter in the apparent separations of pairs of sources of various separations. This rms jitter is a fairly direct measure of the refraction differences induced by the low spatial frequency ionospheric irregularities. For separations greater than 2° , the phase screen corrections dramatically reduce the jitter. Also important is that the rms jitter shows no trends as distance from the phase center increases.

One weakness in our current implementation of this strategy is that the ionosphere is modeled in a piece-wise fashion in time. No “smoothness” constraint is applied to Zernike models from adjoining snapshots. Work is ongoing to rectify this weakness.

In order to assess if (or to what extent) $\phi_{\text{ion,hi}}$ is corrupting our estimate of ϕ_{VLA} , we observe Cyg A multiple times during the course of an observing run. By comparing or, more often, averaging the various estimates of $\phi_{\text{VLA}} + \phi_{\text{ion,hi}}$, we seek to minimize the contribution of $\phi_{\text{ion,hi}}$ to our estimate of ϕ_{VLA} .¹⁵

We close this section with a few general comments on our choice of Zernike polynomials and our implementation. From the work of Jacobson & Erickson (1992a,b) showing

¹⁵This process is implemented in the task SNFLT, a custom-designed task designed to work within AIPS and available from the authors upon request.

that much of the ionospheric structure above the VLA is in the form of waves, one might wonder if a Fourier representation would not be more appropriate. We have chosen to use Zernike polynomials to describe the ionospheric structures precisely because they were invented for the purpose of describing phase errors across a circular aperture. Moreover, compared to a rectangular Fourier transform, many fewer terms of Zernike polynomials are required to describe the ionospheric phase fluctuations. Given the limited sensitivity of the VLA, this criterion is quite important. Finally, although it is not yet contained within our implementation, a natural extension of our method would involve requiring the ionospheric phase corrections to be smooth in time. In order to impose this requirement, one requires an orthogonal basis for the modeling since the interpolation in time is by interpolating the coefficients and this only works if the terms being interpolated are orthogonal.

We emphasize that our division between $\phi_{\text{ion,lo}}$ and $\phi_{\text{ion,hi}}$ is phenomenological and has the effect of making the division based on the order of the Zernike polynomials used rather than on physical properties of the ionosphere. The range of spatial scales in the ionosphere implies that one could use higher-order Zernike polynomials to decompose the phase distortions. In principle, by incorporating a sufficient number of Zernike polynomials one could reduce $\phi_{\text{ion,hi}}$ to a sufficiently low level so as to be unimportant; orders as high as 80 are not unusual for correcting large optical telescopes. However, the number of Zernike coefficients that can be determined is limited by both the sensitivity of the system and the *aperture* distribution of the VLA. The sensitivity of the VLA is an issue because the field must be imaged on less than the ionospheric coherence time, which in turn depends upon the array configuration as the amount of phase contributed by the ionosphere can depend upon the baseline length (Figure 13). In 1 min., a coherence time appropriate for the B configuration, a typical field of view contains no more than 15–20 sources strong enough to be detected; for A configuration, a more typical coherence time is approximately 20 s. Even during times of ionospheric quiescence, fewer than 10 sources may actually be detected; during poor ionospheric “weather” conditions or when sidelobes from strong sources obscure weaker sources, the actual number detected with any confidence may be no more than 5 sources. Hence, in order to avoid (or minimize the occurrence of) spurious Zernike coefficients, we have restricted the modeling to only the $n < 3$ terms. This model of the ionosphere is constructed anew every 1–2 min.

The aperture distribution (as opposed to the more traditional concerns in interferometry regarding the u - v distribution) is related to the range of spatial scales sampled in the ionosphere. In order to characterize large-scale ionospheric structures (e.g., TIDs) that are of concern under typical “weather” conditions, only a modest number of pierce points through the ionosphere are required. In this respect the aperture distribution of the compact configurations (C and D) provides adequate sampling of the relevant spatial scales, though such

sampling is also often not needed because the array remains nearly coherent in these configurations. In contrast, in order to characterize smaller scale ionospheric structures, a high density of closely spaced pierce points is required, which in turn requires high spatial frequencies in the aperture plane, rather than in the u - v plane. In the extended configuration (A and B), the sparseness of the aperture distribution means that small spatial scales are hardly sampled at all. The design of future low frequency instruments may require a compromise between the good uv coverage important for imaging and the good aperture plane coverage that might be required to allow sufficient modelling of small scale ionospheric structure.

4.6. Phase Transfer

Under especially severe ionospheric weather conditions (with ionospheric phase rates on long baselines in excess of 1 deg s^{-1}), it may become necessary to scale the 330 MHz ionospheric-induced phase rates, transfer, and remove them from the 74 MHz data stream (Kassim et al. 1993). In practice, this dual-frequency ionospheric phase transfer technique has been required only rarely, as even in the A configuration phases transferred from a strong source anywhere in the sky retain sufficient coherence on enough short spacings to provide an initial model for self-calibration. Subsequent iterations of self-calibration then improve the phases on the longer baselines. As with straight-forward self-calibration, phase transfer does not compensate for the main failing of self-calibration, which is the lack of an angular dependence on the antenna based phase solutions. However phase transfer may well be of great benefit to future low frequency instruments, especially those planned to operate at lower frequencies and longer baselines than the VLA, such as the LWA (Kassim et al. 2004, 2006b) and LOFAR (Kassim et al. 2004). Therefore it is important that their design does not preclude the possibility of simultaneous observations at multiple frequencies.

4.7. Evolving Techniques of Phase Calibration

The previous sections illustrate successive schemes of ionospheric phase calibration that continue to evolve with real observational experience. A technique such as joint, multi-source self-calibration is required to realize the full potential of emerging larger low-frequency instruments such as the LWA and LOFAR but has yet to be developed and tested. Other related approaches to the calibration of large, low frequency arrays continue to be proposed and discussed (Erickson 2006; Nijboer, Noordam & Yatawatta 2006; Cotton 2006; Brentjens 2005; Noordam 2004; Lane et al. 2004b).

Table 4 presents a simple overview of these evolving schemes; the illustrations in Cotton et al. (2004) may help orient the reader with respect to the applicable geometries.

5. Imaging at Low Frequencies

In this section we summarize the essential procedures needed for effective imaging in the presence of effects that are particularly significant at these low frequencies.

5.1. Confusion and Sidelobes

A key limitation to previous low frequency interferometers operating below 100 MHz has been the poor and confusion-limited sensitivity that arose from their low angular resolution. The high angular resolution of the larger (A- and B-) configurations of the VLA provides some mitigation, but the poor forward gain of the antennas increases the confusion. In fact, two effects are at work, and we distinguish between *classical* confusion and *sidelobe* confusion. The former occurs when the density of sources within the synthesized beam becomes so large that they cannot be separated (e.g., 1 source per every 10 beams is a common criterion for the onset of classical confusion). The latter results from the incompletely removed sidelobe response to bright sources.

Table 5 summarizes the classical confusion limits for the four VLA configurations, where we have taken classical confusion to occur when there is one source per 10 synthesized beams. In order to estimate these classical confusion limits, we have adopted a $\log N$ - $\log S$ relation derived from existing 74 MHz observations,

$$N(> S) = 1.25 \text{ deg}^{-2} \left(\frac{S}{1 \text{ Jy}} \right)^{-1.25} \quad (7)$$

where $N(> S)$ is the areal density of sources, in units of deg^{-2} , stronger than S Jy. Strictly, this $\log N$ - $\log S$ relation is valid only for flux densities $S \gtrsim 0.25$ Jy, based on the flux densities of the sources from which it was determined. Expectations of source densities, based on higher frequency source counts, suggest that this $\log N$ - $\log S$ relation will tend to overestimate the confusion flux density levels, though, and estimates using source counts scaled from higher frequencies give similar results. Even with the uncertainty in the low-frequency $\log N$ - $\log S$ relation, the results presented in Table 5 show that classical confusion is unlikely to limit the sensitivity of 74 MHz observations in the A configuration and probably not in the B configuration (possibly only in crowded regions like the Galactic center), but it is a serious factor for C- and D-configuration observations.

Sidelobe confusion results from the improperly subtracted response to bright sources both inside and outside the main field of view, and is exacerbated when those sources are unresolved by the synthesized beam. The dominant effect is often from the pathologically brightest sources (e.g. Cyg A, Cas A, etc) outside the main field of view whose emission “rumble” through the primary beam sidelobes. This problem is particularly severe for the 74 MHz VLA because of the relatively small aperture ($\approx 6\lambda$) and the sidelobes caused by the feed support structure. Thus the primary antenna gain is low, the primary beam is large (FWHM $\approx 11^\circ$), and the sidelobe levels are high and asymmetric (peak sidelobes are typically only 20 dB down from the main lobe), with a large area of sky in the “close-in sidelobe” region (Figure 6). Moreover, the receiver noise is a small fraction of the total system temperature, so objects all over the sky, including those seen through the sidelobes, produce measurable coherence. Because of this “signal-rich” environment at 74 MHz, it is often necessary to image the entire primary beam and a small number of sources outside it.

Competing factors mitigate the effects of sidelobe confusion, including delay beam and “ionospheric” smearing of the residuals of subtracted sources. Nevertheless remaining artifacts from the few, strongest sources outside the main field of view often limit the sensitivity and dynamic range. Sidelobe confusion can still dominate over classical confusion even in the more compact configurations, since in those cases the arc-minute size scale of the normally offending sources (most notably Cyg A, Cas A, Vir A, Her A, Hyd A, and Tau A) prevents them from being resolved out, and hence their residual effects are worse. (The dominance of sidelobe confusion over thermal noise was indicated earlier in Figures 7 and 8 and discussed in §3. As noted earlier, the sensitivity in the compact configurations is worse than attributable to either form of confusion alone, and our hypothesis is that low-level, broad-band RFI, possibly self-generated, are limiting the performance.

This situation is in direct contrast to that at centimeter wavelengths (Condon et al. 1998, viz. Figure 15) where the receiver temperatures dominate the sky temperature, a more uniform aperture illumination produces lower sidelobes, and the non-thermal spectra result in most sources being fainter than at low frequencies, so that only rarely does one have to contend with sources outside the primary beam.

5.2. Wide-field Imaging

The standard two-dimensional Fourier inversion of visibility data requires that $w\theta^2 \ll 1$ where w is component of the interferometric baseline in the direction of the source and θ is the field of view. This assumption is not valid for 74 MHz observations over any significant

hour angle.¹⁶ Consequently, inverting the visibility data requires either a three-dimensional Fourier inversion or “polyhedral imaging,” in which the field of view is tessellated into facets over which the assumption of a two-dimensional inversion is valid (e.g., Figure 18). For further details and examples, see Cornwell & Perley (1992) and Perley (1999). In general, polyhedral imaging is the more common technique.¹⁷ Table 6 gives general guidelines as to the size and number of facets required for acceptable polyhedral imaging over the entire primary beam. In constructing Table 6 we have made use of the criterion (Thompson et al. 1986; Perley 1999) that the radius of a facet (in radians) should be

$$\theta_{\text{facet}} \approx \frac{1}{3}\sqrt{\theta} \quad (8)$$

where θ is the (FWHM) diameter of the synthesized beam ($\sim \lambda/b$ for a baseline b). Larger facets can be used to reduce the computational burden at the expense of increased phase errors at the edges of the facets.

An alternate strategy, “targeted faceting,” exploits two aspects of the radio astronomical sky. First, the majority of the sidelobe confusion results from the strongest sources either inside or outside the primary beam. The variance in the flux density is given by the expectation value of $S^2N(S)$, which because $N(S) \propto S^x$ with $x < 2$ (equation 7) means that the variance is dominated by the strongest sources. Second, most of the sky remains largely dark (empty of sources), even at these frequencies. Based on these facts, instead of tessellating the entire primary beam, which would take a large amount of time and computer power, one makes use of *a priori* knowledge of the field of view, e.g., from the NVSS or WENSS, to place small facets only where there are sources. We usually have a few hundred small facets per pointing.¹⁸ Depending upon the sensitivity of one’s image and the desired image, this strategy can produce a useful computational savings. Recently, a new technique for wide-field imaging known as the “w-projection” has been proposed. It projects the intrinsically 3-D data onto a 2-D plane with an appropriate Fernel-like convolution, and avoid the teidum involved with polyhedron imaging and targetted faceting. This technique is currently being tested at the VLA (Cornwell, Golap, & Bhatnagar 2006).

¹⁶In general, snapshot observations are not viable with the 74 MHz VLA. The large primary beam and crowded fields means that a snapshot observation produces too few visibilities for an adequate representation of the field of view. The exception is for sources that are so strong, e.g., Cyg A, Vir A, Cas A, that their flux densities dominate the flux densities of other sources in the field of view.

¹⁷The AIPS task IMAGR and the special-purpose, low-frequency imaging task VLAFM implement polyhedral imaging.

¹⁸Determining the location of the facets can be done by the AIPS task SETFC or the special-purpose, low-frequency imaging task VLAFM.

5.3. Astrometry

Even with the relatively large synthesized beam, compared to that attainable at higher frequencies, accurate astrometry at 74 MHz is desired. The astronomical motivations are varied but include spectral index studies, for which one wants to align images obtained at different frequencies (to the extent allowed by any frequency-dependent shifts within the source), and followup at other wavelengths, for which positional accuracies of 1" or better can be required.

If self-calibration is used during phase calibration (§4.4), self-calibration will “freeze” the large-scale refraction but leave the image with an arbitrary absolute position (as in Figure 11). The NVSS or WENSS sources that appear in the image can then be utilized to re-register the astrometry to an accuracy of approximately 5". If the ionosphere is treated as a phase-delay screen (§4.5), the astrometric source grid used in the procedure results in source positions comparable to that of the survey from which the astrometric grid was constructed (e.g., a few arcseconds for NVSS), provided that there are no other systematic effects.

6. Solar Effects, Ionospheric Weather, and Dynamic Scheduling

A potential operational improvement in conducting 74 MHz observations (and low-frequency observations in general) would be to determine when ionospheric conditions are sufficiently quiescent to make useful observations. Currently, observations are scheduled on the telescope well in advance and proceed at the scheduled time. This procedure carries the risk that the ionosphere could be in a sufficiently disturbed state so as to preclude useful observations. A better approach would be to schedule the telescope in a “dynamic” fashion. In order to do this, one would have to conduct a test or identify a proxy observable that could establish the state of the ionosphere rapidly. If the ionosphere was disturbed so that 74 MHz observations would be unlikely to be successful, observations at a higher frequency could proceed with the 74 MHz observations being deferred until such time as the ionosphere is more amenable to correction via methods described here.¹⁹ Our experience suggests a number of ways in which such dynamic scheduling could be implemented.

¹⁹A similar observing strategy is in place for high frequency observations on the VLA (22 and 43 GHz) for which the dominant source of phase fluctuations is the troposphere. In this case, if the tropospheric conditions appear poor, the high frequency observations can be deferred with lower frequency observations being observed instead.

In general, the ionospheric phase effects that dominate calibration issues at low frequencies are a manifestation of highly unpredictable ionospheric weather conditions. The key consideration for low frequency observations is not the total thickness of the ionosphere, as measured by the TEC, but variations in TEC such as TIDs and smaller scale ionospheric structures (§4.5.1). Stable ionospheric conditions can occur at mid-day, when the TEC is highest. At the same time, highly disruptive ionospheric scintillations can occur during the middle of the night. Periods of particular ionospheric instability are [after] sunset and especially sunrise (Figure 14), but it is often easy to avoid observations during these times.

Solar activity can affect 74 MHz observations both directly, due to radio emission from the sun that occur during the daytime, and indirectly, from ionospheric turbulence generated by manifestations of space weather linked to solar activity that can occur any time of the day or night.

At 74 MHz the quiet Sun is a benign 2 kJy disk (compared to Cyg A at 17 kJy), and, at 30' or larger in size, is significantly resolved out with the A and B configurations. However, nonthermal solar radio noise [storms] can have flux densities in excess of 1 MJy, and by entering through the far-out sidelobes of the primary beam render observations completely incapable of being calibrated. However they are usually short-lived, on the order of 30 minutes or less, and can be excised from the data in way similar to the treatment of narrow-band RFI.

The second direct effect is due to the scattering effects of the solar wind. These lead to asymmetric angular broadening and distortion of the brightness distribution of observed sources, and the effects are worst in the A and B configuration when the angular resolution is highest. Experience with both of these direct effects indicates that a useful rule of thumb is to allow at least 60 degree stand-off between the target source and the sun.

The indirect effects are more important since bad ionospheric weather conditions related to a geomagnetic storm precipitated by solar activity can persist for days and render observations useless throughout. One well known manifestation are the massive solar ejections of plasma and magnetic field known as Coronal Mass Ejections (CMEs). Energetic Earth-ward directed CMEs take 20 to 48 hours to arrive and, given a suitable magnetic field orientation, their impact can transfer massive amounts of energy into the upper atmosphere. The resulting geomagnetic storms can damage satellites, knock out power grids, and disrupt communications. Ionospheric disturbances of terrestrial origin, for example acoustic gravity waves can also generate ionospheric variations and poor low frequency observing conditions. However the most severe ionospheric disturbances are usually associated with solar activity.

Various spacecraft and ground-based observatories monitor the Sun, and indices exist to

quantify the level of solar and geomagnetic activity. Hence proxies exist to predict both direct and indirect effects of solar and geomagnetic activity, and in principle these could be used to provide an "ionospheric weather" forecast to guide low frequency observations. However no systematic effort has been conducted yet to assess the correlation between various indices and satisfactory ionospheric imaging conditions. In the mean time, the self-calibration solution, or short time scale stability of the phase on a few baselines from a short scan on a strong 74 MHz source (Cyg A, Vir A) is the most useful means of determining whether ionospheric weather conditions are suitable for observations. If they are deemed too poor to observe, the observations should be postponed, and conditions revisited on the timescale of several hours, or sooner if monitoring of strong sources can be efficiently built in to a dynamic scheduling system. Only limited attempts have been made to quantify the usefulness of this latter approach; while this procedure appears useful, it may not be able to distinguish excellent ionospheric imaging conditions from only fair conditions.

7. The Future of the 74 MHz System

The 74 MHz system expanded from an initial trial system to an operational component of the VLA. Even so, its sensitivity is limited fundamentally by the VLA's modest collecting area ($\sim 10^4$ m², which translates to $\sim 2 \times 10^3$ m² given the $\sim 15\%$ aperture efficiency at this frequency) and poor sensitivity. Even if the VLA telescopes could be made 50% efficient, and the bandwidths increased significantly (§3), it is not possible for the VLA (or the EVLA or the GMRT) to be more sensitive in plausible integration time ($\lesssim 10$ hrs) than roughly 1 mJy beam⁻¹ at 74 MHz—100 times less sensitive than at 1400 MHz to normal-spectrum objects (i.e., those with spectral indices $\alpha < -0.7$, $S_\nu \propto \nu^\alpha$).

The only way to achieve a sensitivity at these wavelengths comparable to that available at centimeter wavelengths is to build a system with much greater collecting area. The Long Wavelength Array (LWA²⁰, Kassim et al. 2006a,b; Taylor 2006; Kassim & Erickson 1998), Low-Frequency Array (LOFAR²¹, Kassim et al. 2001, 2004; Falcke 2005) and Mileura Widefield Array (MWA²², Morales et al. 2006; Bowman et al. 2007) seek to accomplish this at different levels, with different collecting areas, spatial resolutions and frequency ranges. The objective of these projects is to produce aperture synthesis instruments, operating at frequencies between 10 and 300 MHz, with collecting areas of up to $\sim 10^6$ m² at 20 MHz with

²⁰lwa.unm.edu

²¹www.lofar.org

²²www.haystack.mit.edu/ast/arrays/mwa/

maximum baselines of up to 500 km or longer. As such, they would have considerably more collecting area than the VLA (and more than any other previous low-frequency telescope as well) and angular resolutions comparable to that of the VLA at frequencies near 1 GHz.

These projects must take into account the lessons learned from previous low frequency instruments. Here we emphasize some of these lessons, which became apparent during the deployment of the 74 MHz VLA system:

- The system should be designed with careful attention to the signals it emits so that the instrument does not pollute itself with RFI.
- The complex gain and noise temperature of each antenna should be monitored continuously. Measurements of the round-trip phase through the system should also be available.
- Channel bandwidths should be kept small ($\Delta\nu/\nu \ll 1$) so as to avoid strong terrestrial transmitters as often occur at low frequencies and to enable wide-field imaging.
- Wide-band receiving systems should be employed so that more than a single frequency can be observed. Compare the VLA to the CLRO in Figures 1 and 2.
- Large, well-filled primary collectors (presumably composed of numerous individual dipole antennas phased together) should be used so as to produce a primary beam with high forward gain.
- Ionospheric calibration should be considered during the design of the array. In particular, adequate ionospheric calibration may require good *aperture*-plane coverage, rather than good *u-v* plane coverage usually sought in synthesis imaging. Also, the ability to make simultaneous measurements at widely spaced frequencies (for phase transfer) and pointing positions (for modelling the ionosphere over the array) should be available. Rapid (≤ 10 sec) switching may suffice over true simultaneous measurements, given sufficient sensitivity to track ionospheric changes on short time scales.

8. Conclusions

We have described the 74 MHz system that is installed on the NRAO Very Large Array and the Pie Town antenna of the Very Long Baseline Array. All 29 antennas have been outfitted with 74 MHz receivers. With these low-frequency receivers and in the VLA's A configuration, the VLA is the world's highest resolution, highest dynamic range interferometer operating below 150 MHz. Working in conjunction with the PT antenna, the VLA-PT

interferometer, with baselines approaching 70 km, represents the longest baselines ever used for connected element synthesis imaging below 150 MHz.

The calibration strategy for the 74 MHz VLA incorporates a number of features not common at higher frequencies. Chief among these is the importance of the isoplanatic patch size relative to the primary beam diameter. At 74 MHz, the isoplanatic patch size is determined by the ionosphere and the size of the array, particularly in its larger configurations, and can be smaller than the primary beam. We have developed new *field-based* methods of calibrating 74 MHz VLA data that are not restricted to assuming that a single phase correction must apply to the entire field of view. For certain types of observations, e.g., a field dominated by a single strong source that itself is the object of interest, normal, position-independent self-calibration (such as is used at centimeter-wavelengths) can be employed to obtain images with reasonable dynamic ranges. We have presented snapshot images of 3C sources of moderate strength as examples of routine, angle-invariant calibration and imaging, and a sub-sample of these sources with previously well determined low frequency spectra indicate that the 74 MHz flux scale at the Very Large Array is stable and reliable to at least 5 percent. The absolute flux density scale is tied to a model of Cygnus A with a flux density fixed to the Baars et al. (1977) value.

Other aspects of calibration and imaging are not unique to 74 MHz but assume greater importance relative to higher frequencies. For instance, at 1400 MHz one can observe in a pseudo-continuum mode (i.e., low spectral resolution mode) in order to maintain a large field of view, to identify RFI, or both. At 74 MHz, the internal RFI is sufficiently bad that a pseudo-continuum mode (with somewhat higher spectral dynamic range than used typically at 1400 MHz) is essential. Similarly, at 1400 MHz there are typically other sources in the field of view, and it is possible for there to be strong sources outside the field of view that must be CLEANed in order that their sidelobes do not reduce the dynamic range in the image. At 74 MHz, the presence of many sources in the field of view and of strong sources outside the field of view is guaranteed.

Although we expect that the 74 MHz system will continue to be a productive, “facility-level” system of the VLA (and EVLA) for many more years, we also anticipate that the 74 MHz system will be superseded eventually by LOFAR and the LWA and possibly the low-frequency end of the Square Kilometer Array (SKA). Nonetheless, we believe that it offers many lessons for these future high resolution telescopes, as well as the apparatus to explore new science in its own right.

We have benefited from discussions with many individuals. A partial listing includes M. Bietenholz, K. Blundell, C. Brogan, T. Clarke, J. Condon, K. Dyer, T. Ensslin, C. Lacey,

W. Tschager, and K. Weiler. The National Radio Astronomy Observatory is a facility of the National Science Foundation operated under cooperative agreement by Associated Universities, Inc. ASC and WML were supported by National Research Council-NRL Research Associateships. Basic research in radio astronomy at the NRL is supported by 6.1 base funding.

A. Snapshot Observations of Bright Sources

The prototype 8-antenna 74 MHz system (Kassim et al. 1993) was capable of imaging only the dozen or so strongest sources in the sky whose flux densities were hundreds to thousands of Janskys. After the full deployment of the VLA 74 MHz system, a multi-configuration snapshot survey of sources from the 3C catalog was started. Observations were obtained in a succession of three VLA configurations in 1998, A configuration 7-8 March, B configuration 4-5 October, and C configuration 21 November and 4-5 December. Data in both circular polarizations was obtained simultaneously in 1 IF each at 74 and 330 MHz. The data were obtained in spectral line mode with 32 channels at 74 MHz and 64 channels at 330 MHz after online Hanning smoothing. The total available bandwidth was ~ 1.5 and ~ 3 MHz at 74 and 330 MHz, respectively.

All sources were observed numerous times in cycling snapshot fashion to maximize the hour angle coverage. Our typical scan lengths were 5-10 minutes. Many of the sources were sufficiently small in angular extent that the A configuration run was sufficient to generate a good image. More extended sources required B and sometimes C array data, especially at 330 MHz, because of the higher intrinsic angular resolution. Table 7 summarizes the observations and the final image beams at 74 and 330 MHz. Notice that in most cases we convolved the final images with a gaussian, to produce a circular beam.

The data reduction followed the prescriptions described in the previous sections of this paper. All of the images were produced from multiple snapshot observations using an angle-invariant calibration (self-calibration) strategy, which is sufficient for these strong sources because they dominate the self-calibration solution and sidelobe confusion can be ignored. In some cases, work is underway to produce even higher resolution, higher dynamic range images. Superior images are readily obtained with full synthesis observations as compared to the snapshot images presented here.

Because of the calibration method used, the locations of the 330 and 74 MHz images are uncertain due to ionospheric wander. We used scaled subtractions ($330 \text{ MHz} - \alpha_{\text{ave}} \times 73 \text{ MHz}$) to test for shifts between the maps and adjusted the 74 MHz images to agree with

those at 330 MHz. Note that 330 MHz astrometry could be off by as much as $5''$ from the true radio reference frame. Alternatively, by using positions from the NVSS survey one can achieve positional accuracies of $\sim 1''$ at this frequency.

Figure 20 shows 74 and 330 MHz images of a variety of moderately resolved 3C sources with flux densities on the scales of tens of Janskys or higher. Images such as these can now be made routinely with snapshot observations of tens of minutes or less. In most cases these are the first sub-arcminute images of these sources below 100 MHz. Table 8 reports the peak brightness and flux density of the source, but, for the resolved sources for which we present images, these values may be lower limits, as some of the flux may have been resolved out. We discuss the resolved sources briefly but make no quantitative analyzes, as our discussion here is intended only to be illustrative.

3C 10 Figure 20*a* shows the images of Tycho’s supernova remnant at 74 and 330 MHz. We can see in these images a limb-brightened spherical shell with a diameter of $\sim 8'$, and enhanced emission toward the NE half of the shell. This structure is similar to that observed at 330 MHz and 1.4 GHz by Katz-Stone et al. (2000), and at 610 MHz by Duim & Strom (1975).

3C 33 Figure 20*b* presents the 330 and 74 MHz images of this radio galaxy. The 74 MHz image shows the lobes and fainter emission between these two structures. The 330 MHz image resolves some of the details of this source, separating each lobe into 2 components, as well as showing diffuse emission extending perpendicular to the jet axis in regions between the lobes and the nucleus. The structures seen in our images are similar to the ones seen at 1.5 GHz by Leahy, & Perley (1991). A low resolution 160 MHz image of this source (Slee 1977) was able to resolve it only into two components.

3C 84 Figure 20*c* shows the 74 MHz image of the central regions of the Perseus cluster, which contains a number of strong radio sources including 3C 84. An enlarged plot of the 330 MHz Figure 20*d* image of this radio galaxy shows a strong core, two lobes in the N-S direction and some extended emission beyond the lobes. These structures are similar to the ones detected by Pedlar, A. et al. (1990) at 1.4 GHz, 330 MHz and 151 MHz. The 74 MHz image does not resolve the nucleus and lobes, but shows some diffuse emission extending to the NW and SW, corresponding to previous outbursts (see Fabian et al. (2002) for a more detailed discussion of this image and the relation between these structures and X-ray holes).

3C 98 Figure 20*e* The 74 MHz image shows a double lobe structure with diffuse emission in between. The 330 MHz image shows a similar structure, although with higher resolution, allowing the detection of the hotspots and part of the jet. These structures

were previously imaged at higher frequencies (1.4 and 4.8 GHz) by Leahy et al. (1997) and Young et al. (2005). A 160 MHz image of this galaxy was presented by Slee (1977).

- 3C 129** Figure 20*f* shows 3C 129 at 74 MHz. A study of the 330 MHz image (Lane et al. 2002) have confirmed the existence of a steep-spectrum “crosspiece” at the head of 3C 129, along the NE-SW direction, perpendicular to its main tail. This structure was previously detected at 600 MHz (Jaegers & de Grijp 1983) and have recently been observed by Lal & Rao (2004) with the GMRT at 240 and 610 MHz. We see no indication of this structure at 74 MHz, but our resolution is considerably lower, so it is probably blended with the head of 3C 129.
- 3C 144** Figure 20*g* shows 3C 144 (the Crab Nebula, Tau A) at 74 MHz and 330 MHz. This source can be used as an amplitude calibrator in more compact configurations (C and D). The 74 MHz compact source in the center of the nebula is the Crab pulsar (PSR B0531+21). A higher sensitivity 330 MHz image of this source is presented by Frail et al. (1995), while Bietenholz et al. (1997) present a study of the 74/330 MHz radio spectral index and find evidence for intrinsic thermal absorption.
- 3C 218 (Hydra A)** Figure 20*h* present the 330 and 74 MHz images of Hydra A, where we can see that this radio galaxy has a complex structure, consisting of several outbursts. Lane et al. (2004a) present a detailed study of this source, the spectral indices of the different components and their correlation of the X-ray emission from the cluster of galaxy where it resides.
- 3C 219** The 74 MHz emission from this radio galaxy (Figure 20*i*) shows two lobes and diffuse emission between them. This emission is resolved into better detail by the 330 MHz image, where we can see the N and S hotspots, the jet and some diffuse emission. These structures are similar to the ones seen at 1.4 GHz by Clarke et al. (1992).
- 3C 274 (Vir A)** Figure 20*j* shows 3C 274 (Vir A), one of the sources that can be used as a primary bandpass and flux density calibrator, in addition to or instead of Cyg A (particularly if Cyg A is not above the horizon). Both 330 MHz and 74 MHz images show a complex structure, indicative of the interaction between the radio plasma and the intra cluster medium. A more detailed discussion about the 330 MHz image of this source is presented by Owen et al. (2000).
- 3C 327** The 74 MHz image of this galaxy (Figure 20*k*) shows a double structure along the E-W direction. The E component is elongated, indicating the presence of multiple components. A low resolution 160 MHz image from Slee (1977) showed only two blobs

along the E-W direction. The structure seen at 74 MHz are confirmed by the 330 MHz image, where we can clearly see the hotspots and some diffuse emission, similar to the structure observed at 8.4 GHz by Leahy et al. (1997).

3C 353 The 74 MHz image of this radio galaxy (Figure 20*l*) is broken into 3 components aligned along the E-W direction. Previous low frequency (160 MHz) images by Slee (1977) were not able to detect multiple components, detecting only an extended source in the E-W direction. The 330 MHz image shows the hotspots and diffuse emission in the lobes, similar to the structure detected by Baum et al. (1988) at 5 GHz.

3C 390.3 In Figure 20*m* we can see that the 74 MHz image of this radio galaxy is resolved into 2 lobes and diffuse emission associated with them. This structure is similar to the one detected at 610 MHz by radio Jaegers (1987), using WSRT observations. The 330 MHz image shows the hotspots and diffuse emission in better detail, as well as the nucleus. The structures seen at this frequency are similar to the ones detected with 1.4 GHz VLA observations (Leahy & Perley 1995).

3C 392 Figure 20*n* presents the images of this supernova remnant, which has similar structure at 74 and 330 MHz. The 330 MHz image shows details similar to the ones seen at 1.4 GHz (Jones, Smith & Angellini 1993; Giacani et al. 1997). Higher resolution, full synthesis images at both frequencies of this SNR, also known as W44, are presented in Castelletti et al. (2007).

3C 405 (Cyg A) Figure 20*o* shows our primary bandpass and flux density calibrator, 3C 405 or Cyg A. This image is dynamic range limited. 3C405 is almost unresolved at 74 MHz, however, higher resolution (VLA + Pie Town) images at both 74 and 330 MHz are presented by Lazio et al. (2006). The VLA 330 MHz image is able to resolve the emission into hotspots and associated diffuse emission, similar to the structure detected by Perley & Erickson (1984) at 1.4 GHz, although without the detection of the nucleus and the jets.

3C 445 Figure 20*p* shows that 74 MHz image of this radio galaxy is composed of two bright lobes and some faint extended emission around the nucleus. A lower resolution 160 MHz image of this galaxy (Slee 1977) shows only three blobs. The VLA 330 MHz image resolves the lobes into hotspots and some associated diffuse emission, similar to that observed at higher frequencies (Kronberg, Wielebinski & Graham 1986; Leahy et al. 1997).

3C 452 The 74 MHz image of this radio galaxy is presented in Figure 20*q*, which shows a double lobed structure, similar to the one detected at 610 MHz by Jaegers (1987),

using WSRT. The 330 MHz image resolves the structure of this galaxy into better detail, hotspots and diffuse emission along the jet, similar to the structure detected at 1.4 GHz by Dennett-Thorpe, et al. (1999).

3C 461 Figure 20*r* shows the 74 and 330 MHz of Cas A, another source that can be used as a primary bandpass and flux density calibrator in more compact configurations (C and D). The 330 and 74 MHz images look similar, although of lower resolution compared to the 1.4 GHz images presented in Anderson et al. (1991). Kassim et al. (1995) found evidence of internal thermal absorption using the prototype 8-antenna system, that was subsequently confirmed by Delaney et al. (2004) using the full 74 MHz VLA + PT Link (Figure 21). These observations were obtained with a maximum baseline is 72 km, corresponding to an angular resolution of 8.5".

REFERENCES

- Alfvén, H. & Herlofson, N. 1950, *Phys. Rev.*, 78, 616
- Anderson, M., Rudnick, L., Leppik, P., Perley, R., & Braun, R. 1991, *ApJ*, 373, 146
- Baars, J. W. M., Genzel, R., Pauliny-Toth, I. I. K., & Witzel, A. 1977, *A&A*, 61, 99
- Baum, S. A., Heckman, T. M., Bridle, A., van Breugel, W. J. M., & Miley, G. K. 1988, *ApJS*, 68, 643
- Bietenholz, M. F., Kassim, N., Frail, D. A., Perley, R. A., Erickson, W. C., & Hajian, A. R. 1997, *ApJ*, 490, 291
- Bowman, J. D. et al. 2007, *AJ*, in press
- Braude, S. Ia., Men, A. V., & Sodin, L. G. 1978, *Antenny*, 26, 3
- Brentjens, M. A., 2005, *Astron. Nachr.*, 326, 609-609
- Bridle, A. H. 1999, in *Synthesis Imaging in Radio Astronomy*, eds. R. A. Perley, F. R. Schwab, & A. H. Bridle (ASP: San Francisco) p. 443
- Bridle, A. H. & Purton, C. R. 1968, *AJ*, 73, 717
- Bock, D. C.-J., Large, M. I., & Sadler, E. M. 1999, *AJ*, 117, 1578
- Castelletti, G., Dubner, G., Brogan, C., Kassim, N. E. *A&A*, in press (astro-ph/0702746)

- Clarke, D. A., Bridle, A. H., Burns, J. O., Perley, R. A., & Norman, M. L. 1992, *ApJ*, 385, 173
- Cohen, A.S., Lane, W.M., Kassim, N.E., Lazio, T.J.W., Cotton, W.D., Condon, J.J., Perley, R.A., Erickson, W.C. 2006, in "From Clark Lake to the Long Wavelength Array: Bill Erickson's Radio Science", ASP Conference Series, Vol. 345, Proceedings of the Conference held 8-11 September, 2004 in Santa Fe, New Mexico, USA. Edited by N. Kassim, M. Perez, M. Junor, and P. Henning, p.299.
- Cohen, A. S., Röttgering, H. J. A., Kassim, N. E., et al. 2003, *ApJ*, 591, 640
- Cohen, A. S., et al. 2007, in preparation
- Condon, J. J., Cotton, W. D., Greisen, E. W., Yin, Q. F., Perley, R. A., Taylor, G. B., & Broderick, J. J. 1998, *AJ*, 115, 1693
- Cornwell, T.J., Golap, K., Bhatnagar, S. in "From Clark Lake to the Long Wavelength Array: Bill Erickson's Radio Science", ASP Conference Series, Vol. 345, Proceedings of the Conference held 8-11 September, 2004 in Santa Fe, New Mexico, USA. Edited by N. Kassim, M. Perez, M. Junor, and P. Henning, p.350.
- Cornwell, T. J. & Fomalont, E. B. 1999, in *Synthesis Imaging in Radio Astronomy II*, eds. G. B. Taylor, C. L. Carilli, & R. A. Perley (ASP:San Francisco) p. 187
- Cornwell, T. J. & Perley, R. A. 1992, *A&A*, 261, 353
- Cotton, W.D. in "From Clark Lake to the Long Wavelength Array: Bill Erickson's Radio Science" ASP Conference Series, Vol. 345, Proceedings of the Conference held 8-11 September, 2004 in Santa Fe, New Mexico, USA. Edited by N. Kassim, M. Perez, M. Junor, and P. Henning, p.337
- Cotton, W. D. & Condon, J. J. 2002, *Proc. URSI General Assembly*, J3.0.2
- Cotton, W. D., Condon, J. J., Perley, R. A., Kassim, N., Lazio, J., Cohen, A., Lane, W., & Erickson, W. C. 2004, *Proc. SPIE*, 5489, 180
- Delaney, T., Rudnick, L., Jones, T., Fesen, R., Hwang, U., Petre, R., & Morse, J. 2004, in *X-Ray and Radio Connections Conference Proceedings*, eds. L.O. Sjouwerman and K.K. Dyer. Published electronically by NRAO, <http://www.aoc.nrao.edu/events/xraydio>. Held 3/6 February 2004 in Santa Fe, New Mexico, USA (E4.05)
- Dennett-Thorpe, J., Bridle, A. H., Laing, R. A., & Scheuer, P. A. G. 1999, *MNRAS*, 304, 271

- Duim, R. M., & Strom, R. G. 1975, *A&A*, 39, 33
- Erickson, W. C. 1984, *J. Astrophys. Astron.*, 5, 55
- Erickson, W. C., Perley, R. A., Flatters, C., & Kassim, N. E. 2001, *A&A*, 366, 1071
- Erickson, W. C., Mahoney, M. J., & Erb, K. 1982, *ApJS*, 50, 403
- Erickson, W.C. in "From Clark Lake to the Long Wavelength Array: Bill Erickson's Radio Science", ASP Conference Series, Vol. 345, Proceedings of the Conference held 8-11 September, 2004 in Santa Fe, New Mexico, USA. Edited by N. Kassim, M. Perez, M. Junor, and P. Henning, p.317
- Fabian, A. C., Celotti, A., Blundell, K. M., Kassim, N. E., & Perley, R. A. 2002, *MNRAS*, 331, 369
- Falcke, H. 2005, *Astron. Nachr.*, 326, 612
- Frail, D. A., Kassim, N. E., Cornwell, T. J., & Goss, W. M. 1995, *ApJ*, 454, L129
- Giacani, E. B., Dubner, G. M., Kassim, N. E., Frail, D. A., Goss, W. M., Winkler, P. F., & Williams, B. F. 1997, *AJ*, 113, 1379
- Gizani, Nectaria A. B., Cohen, A., Kassim, N. E., 2005 *MNRAS*, 358, 1061
- Golap, K., Cornwell, T.J., Perley, R.A., Bhatnagar, S. in "From Clark Lake to the Long Wavelength Array: Bill Erickson's Radio Science", ASP Conference Series, Vol. 345, Proceedings of the Conference held 8-11 September, 2004 in Santa Fe, New Mexico, USA. Edited by N. Kassim, M. Perez, M. Junor, and P. Henning, p.366.
- Hewish, A., Bell, S. J., Pilkington, J. D. H., Scott, P. F., & Collins, R. A. 1968, *Nature*, 217, 709
- Jansky, K. G. 1935, *Proc. I. R. E.*, 23, 1158
- Jacobson, A. R. & Erickson, W. C. 1992a, *Planetary and Space Sci.*, 40, 447
- Jacobson, A. R. & Erickson, W. C. 1992b, *A&A*, 257, 401
- Jägers, W. J. 1987, *A&AS*, 67, 395
- Jägers, W. J., & de Grijp, M. H. K. 1983, *A&A*, 127, 235
- Jones, L. R., Smith, A., & Angellini, L. 1993, *MNRAS*, 265, 631

- Kassim, N. E., & Erickson, W. C. 1998, Proc. SPIE, 3357, 740
- Kassim, N. E., et al. 2006, Long Wavelength Astrophysics, 26th meeting of the IAU, Joint Discussion 12, 21 August 2006, Prague, Czech Republic, JD12, #56, 12
- Kassim, N. E., Lazio, T. J. W., Erickson, W. C., et al. 2000, in Radio Telescopes, Proc. SPIE, ed. H. R. Butcher, vol. 4015, p. 328
- Kassim, N. E., Perley, R. A., Dwarakanath, K. S., Erickson, W. C. 1995, ApJ, 455, L59
- Kassim, N. E., Perley, R. A., Erickson, W. C., & Dwarakanath, K. S. 1993, AJ, 106, 2218
- Kassim, N. E., Lazio, T. J. W., Ray, P. S., Crane, P. C., Hicks, B. C., Stewart, K. P., Cohen, A. S., Lane, W. M., 2004, Planetary and Space Science, Volume 52, Issue 15, p. 1343-1349
- Kassim, N. E. 1988, ApJS, 68, 715
- Kassim, N. E., Polisensky, E. J., Clarke, T. E., Hicks, B. C., Crane, P. C., Stewart, K. P., Ray, P. S., Weiler, K. W., Rickard, L. J., Lazio, T. J. W., Lane, W. M., Cohen, A. S., Nord, M. E., Erickson, W. C., Perley, R. A. in "From Clark Lake to the Long Wavelength Array: Bill Erickson's Radio Science", ASP Conference Series, Vol. 345, Proceedings of the Conference held 8-11 September, 2004 in Santa Fe, New Mexico, USA. Edited by N. Kassim, M. Perez, M. Junor, and P. Henning, p.392
- Katz-Stone, D. M., Kassim, N. E., Lazio, T. J. W., O'Donnell, R. 2000, ApJ, 529, 453
- Kiepenheuer, K. O. 1950, Phys. Rev., 79, 738
- Kronberg, P. P., Wielebinski, R., & Graham, D. A. 1986, A&A, 169, 63
- Krymkin, V. V. & Sidorchuk, M. A. 1994, Ap&SS, 213, 1
- Kühr, H., Witzel, A., Pauliny-Toth, I. I. K., & Nauber, U. 1981, A&AS, 45, 367
- Lane, W. M., Clarke, T. E., Taylor, G. B., Perley, R. A., Kassim, N. E. 2004, AJ, 127, 48
- Lane, W. M., Kassim, N. E., Enßlin, T. A., Harris, D. E., & Perley, R. A. 2002, AJ, 123, 2985
- Lane, W., Cohen, A., Cotton, W. D., Condon, J. J., Perley, R. A., Lazio, J., Kassim, N., Erickson, W. C. in "Ground-based Telescopes". Edited by Oschmann, Jacobus M., Jr. Proceedings of the SPIE, Volume 5489, pp. 354-361 (2004)

- Lane, W. M., Cohen, A. S., Kassim, N. E., Lazio, T. J. W., Perley, R. A., Cotton, W. D., Greisen, E. W., *Radio Science*, 40, RS5S05, 2005. (See also Golap et al. 2006.)
- Lane, W.M., Cohen, A.S., Kassim, N.E., Lazio, T.J.W., in "From Clark Lake to the Long Wavelength Array: Bill Erickson's Radio Science", ASP Conference Series, Vol. 345, Proceedings of the Conference held 8-11 September, 2004 in Santa Fe, New Mexico, USA. Edited by N. Kassim, M. Perez, M. Junor, and P. Henning, p.203.
- Lal, D.V., & Rao, A. P. 2004, *A&A*, 420, 491
- Lazio, T. J. W., Cohen, A. S., Kassim, N. E., Perley, R. A., Erickson, W. C., Carilli, C. L., & Crane, P. C. 2006, *ApJ*, 642, L33
- Leahy, J. P., Black, A. R. S., Dennett-Thorpe, J., Hardcastle, M. J., Komissarov, S., Perley, R. A., Riley, J. M., & Scheuer, P. A. G. 1997, *MNRAS*, 291, 20
- Leahy, J. P., Muxlow, T. W. B., & Stephens, P. W. 1989, *MNRAS*, 239, 401
- Leahy, J. P. & Perley, R. A. 1991, *AJ*, 102, 537
- Leahy, J. P., & Perley, R. A. 1995, *MNRAS*, 277, 1097
- Mills, B. Y. 1952, *Aust. J. Sci. Res.*, A5, 456
- McCready, L. L., Pawsey, J. L., & Payne-Scott, R. 1947, *Proc. Royal Soc. A*, 190, 357
- Morales, M.F., Lonsdale, C.J., Cappallo, R.J., Hewitt, J.N., Doeleman, S., in "From Clark Lake to the Long Wavelength Array: Bill Erickson's Radio Science", ASP Conference Series, Vol. 345, Proceedings of the Conference held 8-11 September, 2004 in Santa Fe, New Mexico, USA. Edited by N. Kassim, M. Perez, M. Junor, and P. Henning, p. 452.
- Nijboer, R. J., Noordam, J. E., Yatawatta, S. B. in "Astronomical Data Analysis Software and Systems XV" ASP Conference Series, Vol. 351, Proceedings of the Conference Held 2-5 October 2005 in San Lorenzo de El Escorial, Spain. Edited by Carlos Gabriel, Christophe Arviset, Daniel Ponz, and Enrique Solano. San Francisco: Astronomical Society of the Pacific, 2006., p.291
- Noordam, J.E. 2004, in "Ground-based Telescopes". Edited by Oschmann, Jacobus M., Jr. Proceedings of the SPIE, Volume 5489, pp. 817-825
- Pedlar, A., Ghataure, H. S., Davies, R. D., Harrison, B. A., Perley, R., Crane, P. C., & Unger, S. W. 1990, *MNRAS*, 246, 477

- Napier, P. J., Thompson, A. R., & Ekers, R. D. 1983, *Proc. IEEE*, 71, 1295
- Owen, F. N., Eilek, J. A., & Kassim, N. E. 2000, *ApJ*, 543, 611
- Pawsey, J. L., Payne-Scott, R., & McCready, L. L. 1946, *Nature*, 157, 158
- Perley, R. A. 2002, *Proc. URSI General Assembly*, J4.0.2
- Perley, R. A. 1999, in *Synthesis Imaging in Radio Astronomy II*, eds. G. B. Taylor, C. L. Carilli, & R. A. Perley (San Francisco: ASP) p. 383
- Perley, R. A. & Erickson, W. C. 1984, *VLA Scientific Memorandum #146*
- Reber, G. 1940, *ApJ*, 91, 621
- Rees, N. 1990, *MNRAS*, 244, 233
- Rengelink, R. B., Tang, Y., de Bruyn, A. G., Miley, G. K., Bremer, M. N., Röttgering, H. J. A., & Bremer, M. A. R. 1997, *A&AS*, 124, 259
- Roger, R. S., Costain, C. H., & Stewart, D. I. 1986, *A&AS*, 65, 485
- Ryle, M. 1952, *Proc. Royal Soc. A*, 211, 351
- Ryle, M., Smith, F. G., & Elsemore, B. 1950, *MNRAS*, 110, 508
- Ryle, M. & Vonberg, D. D. 1946, *Nature*, 158, 339
- Shepherd, D. S., Claussen, M. J., & Kurtz, S. E. 2001, *Science*, 292, 1513
- Shkolvsky, I. S. 1952, *AZh*, 29, 418
- Slee, O. B. 1977, *Au. J. Phys. Astron.*, 43, 1
- Slee, O. B. & Higgins, C. S. 1975, *Au. J. Phys. Astron.*, 36, 1
- Slee, O. B. & Higgins, C. S. 1973, *Au. J. Phys. Astron.*, 27, 1
- Subramanian, K. R., Gowda, C. N., Hameed, A. T. A., & Sastry, C. V. 1986, *Astron. Soc. India. Bulletin*, 14, 236
- Swarup, G. 1990, *Indian Journal of Radio and Space Physics*, 19, 493
- Taylor, G. B. 2006, *Long Wavelength Astrophysics*, 26th meeting of the IAU, Joint Discussion 12, 21 August 2006, Prague, Czech Republic, *JD12*, #17, 12,

Thomasson, P. 1986, QJRAS, 27, 413

Thompson, A. R., Moran, J. M., & Swenson, G. W., Jr. 1986, *Interferometry and Synthesis in Radio Astronomy* (Wiley: New York)

Walker, R. C. 1995, in *Very Long Baseline Interferometry and the VLBA*, eds. J. A. Zensus, P. J. Diamond, & P. J. Napier (ASP:San Francisco) p. 247

Yates, K. W. 1968, *Au. J. Phys.*, 21, 167

Young, A., Rudnick, L., Katz, D., DeLaney, T., Kassim, N. E., & Makishima, K. 2005, *ApJ*, 626, 748

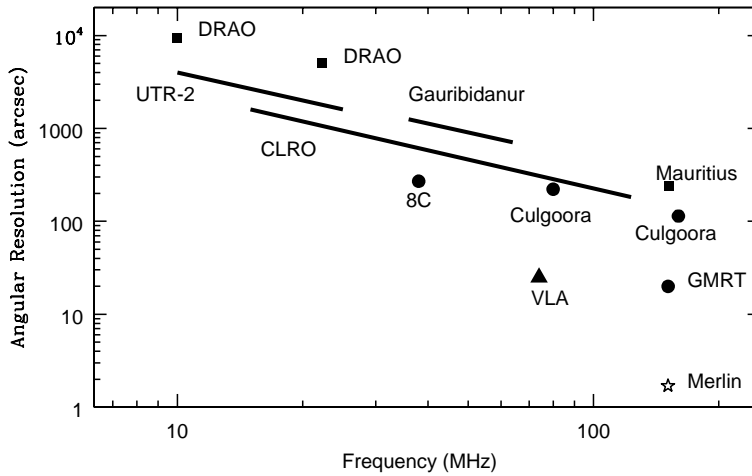


Fig. 1.— Angular resolution (arcseconds) as a function of frequency (MHz) for past and present imaging instruments in the 10 to 200 MHz range. The various telescopes include the UTR-2 (Krymkin & Sidorchuk 1994), Gauribidanur (Subramanian et al. 1986), 8C (Rees 1990), Clark Lake Radio Observatory (CLRO, Kassim 1988), Culgoora (Slee & Higgins 1973, 1975; Slee 1977), Dominion Radio Astrophysical Observatory (DRAO, Bridle & Purton 1968; Roger et al. 1986), MERLIN (Thomasson 1986; Leahy, Muxlow & Stephens 1989) and the Mauritius radio telescope. The 74 MHz VLA is represented by the filled triangle.

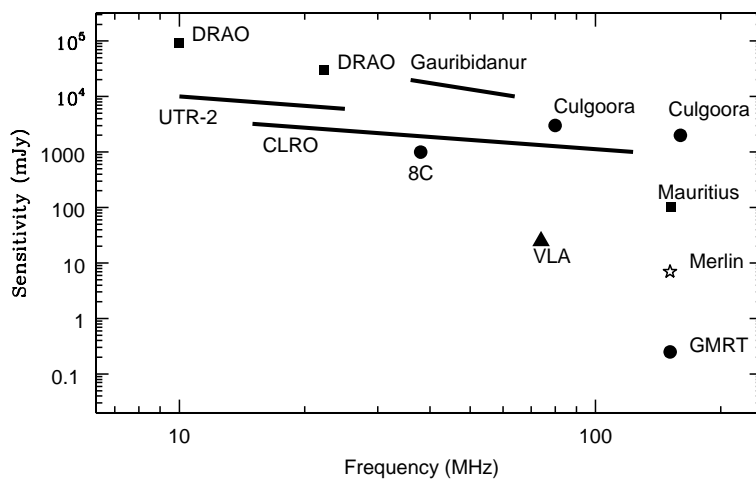


Fig. 2.— Sensitivity (mJy) to a point source as a function of frequency for the same instruments shown in Figure 1. The sensitivities are estimates of the minimum detectable flux density provided by past and present telescopes. The sensitivity of most of the telescopes shown here were or are confusion limited; for the VLA and the GMRT, an integration time of 8 hr was assumed in calculating their sensitivities.

Fig. 3.— A picture of a 74 MHz dipole mounted on a VLA antenna. In the center of the picture is the subreflector, supported by the quadrupod legs. The 74 MHz (crossed) dipoles are in the lower center of the picture. The cable that carries the signals from the dipoles to the receivers drops from the intersection of the dipoles to the bottom of the antenna’s surface. Also visible just below the subreflector are the 330 MHz dipoles.

Fig. 4.— The block diagram of the 74 MHz receiver on the Pie Town VLBA antenna. The receivers on the VLA antennas are similar, with the main difference being that the VLA receivers are not heterodyne receivers. Rather the 74 and 330 MHz signals are transferred directly to the intermediate frequency (IF) transmission system.

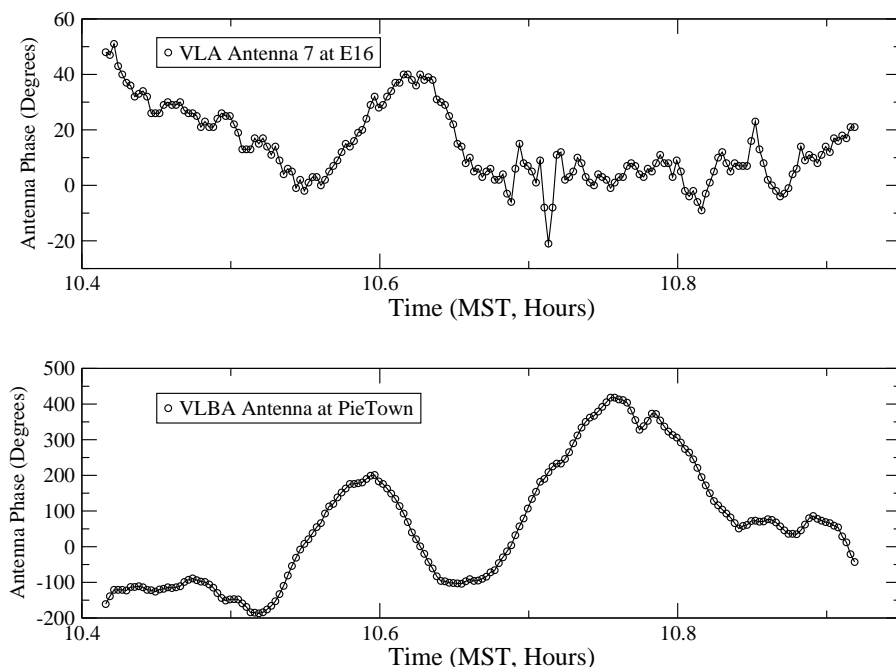


Fig. 5.— First fringes using the PT Link at 74 MHz. The source observed was 3C 123. *Top* Phase as a function of time for VLA antenna #7, located relatively close to the center of the array. *Bottom* Phase as a function of time for the PT antenna. In both cases, the phases are measured relative to an antenna near the center of the array. The scales on the ordinates differ.

Fig. 6.— The primary beam power pattern at 74 MHz from one of the antennas. Other antennas have similar power patterns. The left panel shows the left circular polarization, and the right panel shows the right circular polarization. The axes are the sines of the offset angle. The contours show the decrease, in dB, from the peak of the pattern (drawn at 3, 6, 10, 15, 20, 25, and 30 dB levels). The sharp edge on the right hand side of the plots results from the motion limits on pointing for the VLA antennas.

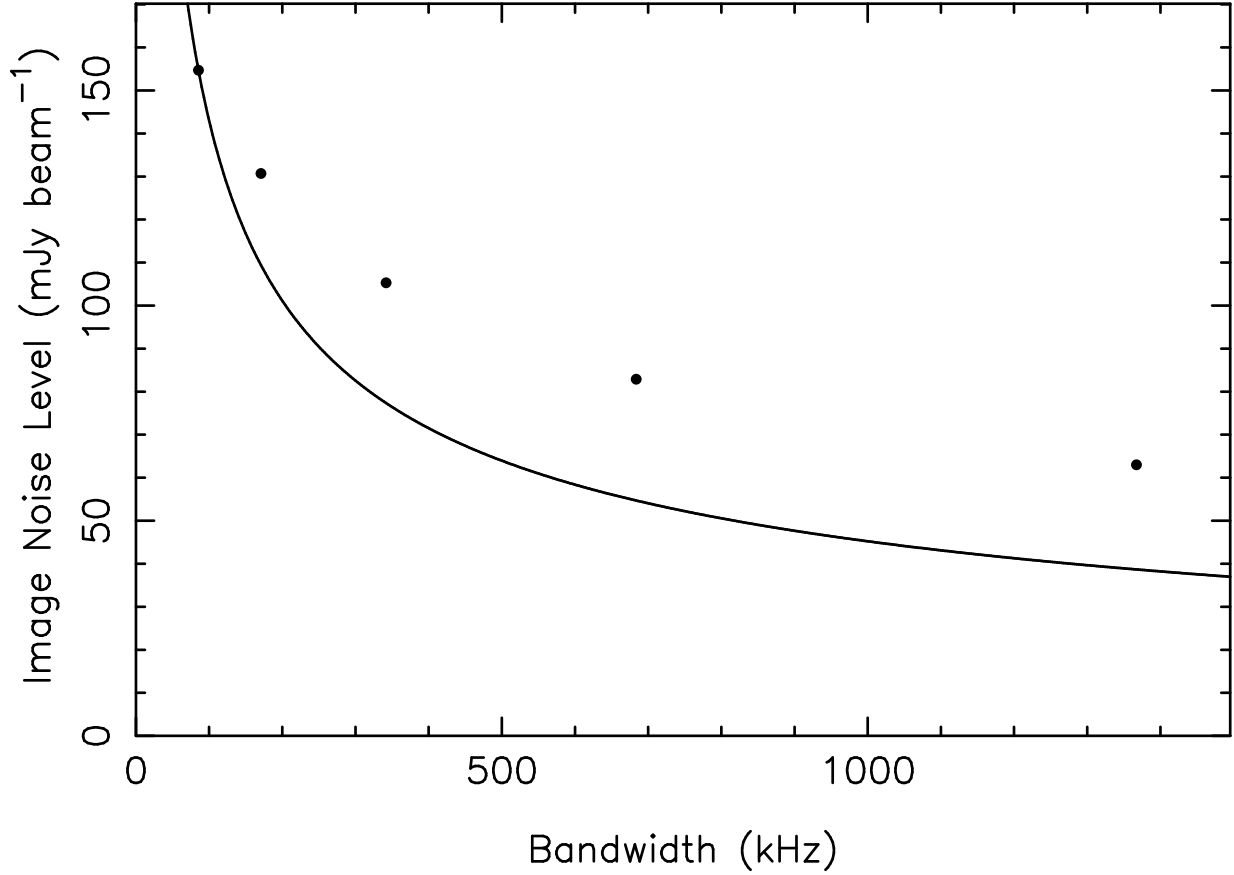


Fig. 7.— The rms image noise level as a function of receiver bandwidth. The dots show the measured values from a 90 min. integration calibrated and imaged in the fashion described in §§4 and 5. The solid line shows the behavior expected, $\Delta\nu^{-1/2}$, if the system performance is limited by thermal noise. This behaviour is typical of observations obtained in the A and B configurations.

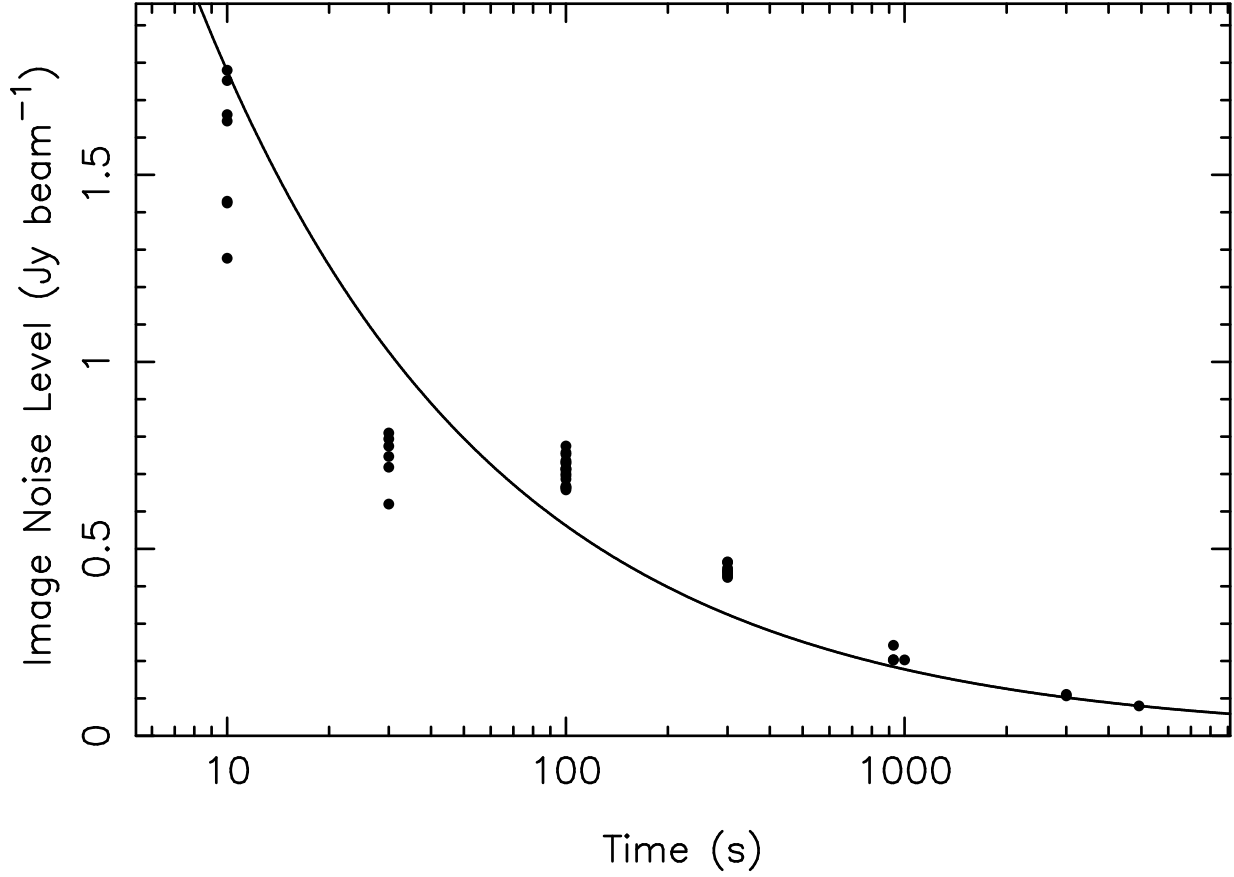


Fig. 8.— The rms image noise level as a function of integration time. Multiple points at the same integration time indicate integration times for which multiple, independent images were constructed from the approximately 1-hr total integration time. The solid line shows the behavior expected, $t^{-1/2}$, if the system performance is limited by thermal noise. This behaviour is typical of observations obtained in the A and B configurations.

Fig. 9.— A demonstration of the excision of 74 MHz RFI. *Left:* The visibility amplitudes on a single baseline are displayed in a (linear) gray scale format with frequency on the abscissa and time on the ordinate. The time axis is not linear, and the thick horizontal black stripes indicate times when other sources were being observed. The bright vertical stripes represent the 100 kHz “comb”. The strength of the comb varies from baseline to baseline and as a function of time within individual baselines, depending upon the orientation of the antennas and how strongly they couple. For this illustration, we have chosen a particularly severe example; there were other baselines in the same data set for which the comb was barely visible. *Right:* The same data after RFI have been flagged with FLGIT. This panel shows a much more homogeneous brightness distribution than the one to the left, indicating that most of the RFI (strongest interference) was removed.

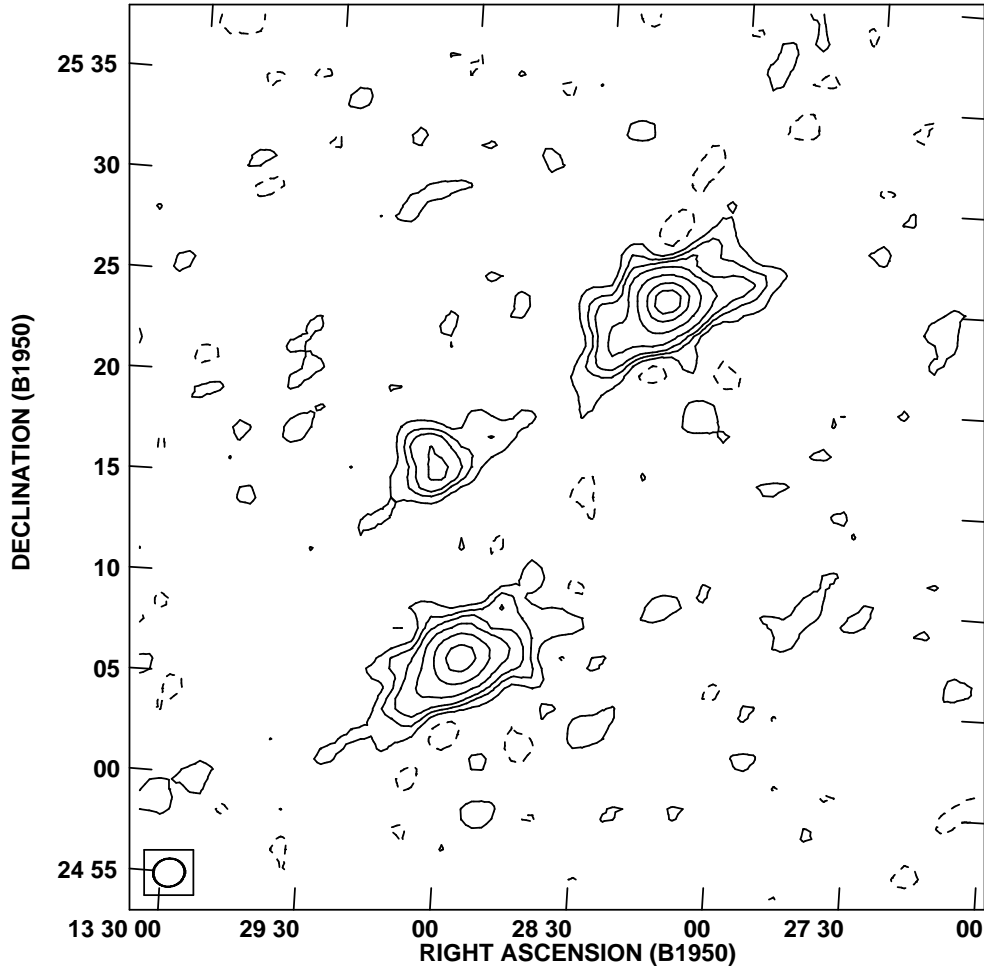


Fig. 10.— An example of the distortions introduced by imaging a region larger than the isoplanatic patch. This image is a subimage of a larger image. The sources shown are roughly 7° from the phase center of the larger image; the two brightest sources should be point-like or nearly so while the third, fainter source is extended, with a nearly north-south orientation. The image was produced from combined B- and C-configuration observations; the beam is $95'' \times 83''$ and is shown in the lower left. The rms noise level in the image is approximately 30 mJy beam^{-1} , and the contour levels are $30 \text{ mJy beam}^{-1} \times -4, -2, 2, 4, 6, 10, 20, 40, 60, 100,$ and 150 . The bandwidth and time averaging used in producing this image are sufficiently small that both contribute a negligible amount (< 1 beamwidth) of smearing.

Fig. 11.— An illustration of the position offsets arising from phase distortions caused by the largest spatial structures ($\gtrsim 1000$ km) in the ionosphere. The contours show the 74 MHz image; the gray scale is an overlay of the NVSS in this region. The NVSS is at a sufficiently high frequency that the ionospheric refraction is much less than a beamwidth. Note that not all NVSS sources have a 74 MHz counterpart.

Fig. 12.— The temporal variation in the refractive shift caused by the largest spatial scales in the ionosphere. Shown is the offset, in both right ascension and declination, of Cyg A from its known position as a function of time, with a 1 min. sampling interval. These observations were taken in the B configuration.

Fig. 13.— An illustration of the phase distortions caused by ionospheric mesoscale structure, in this case a traveling ionospheric disturbance (TID), with the typical scale of order hundreds of kilometers. Shown are the phases, measured relative to an antenna near the center of the array, as a function of time for three antennas along the west arm of the array.

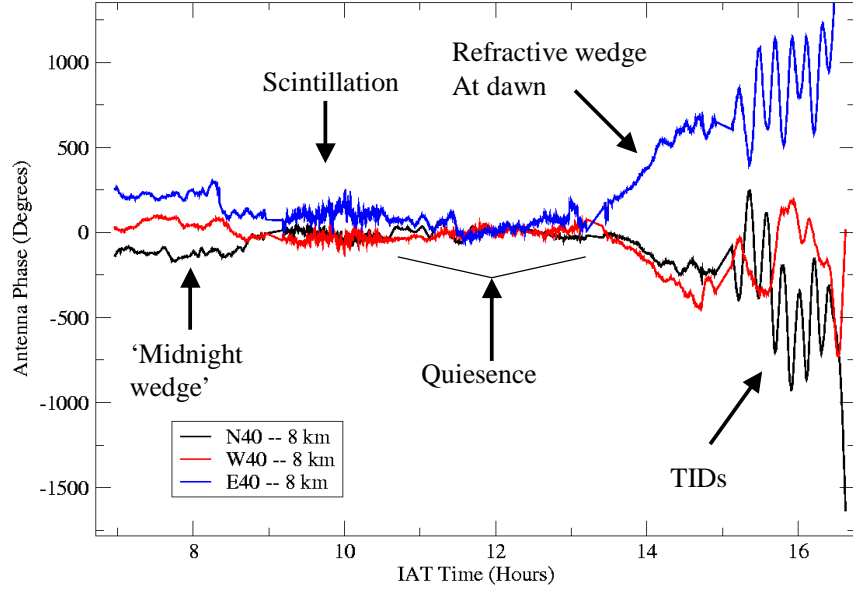
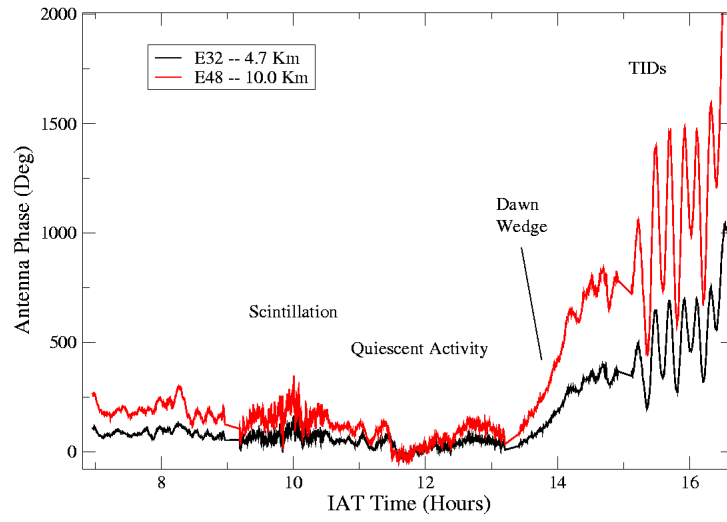
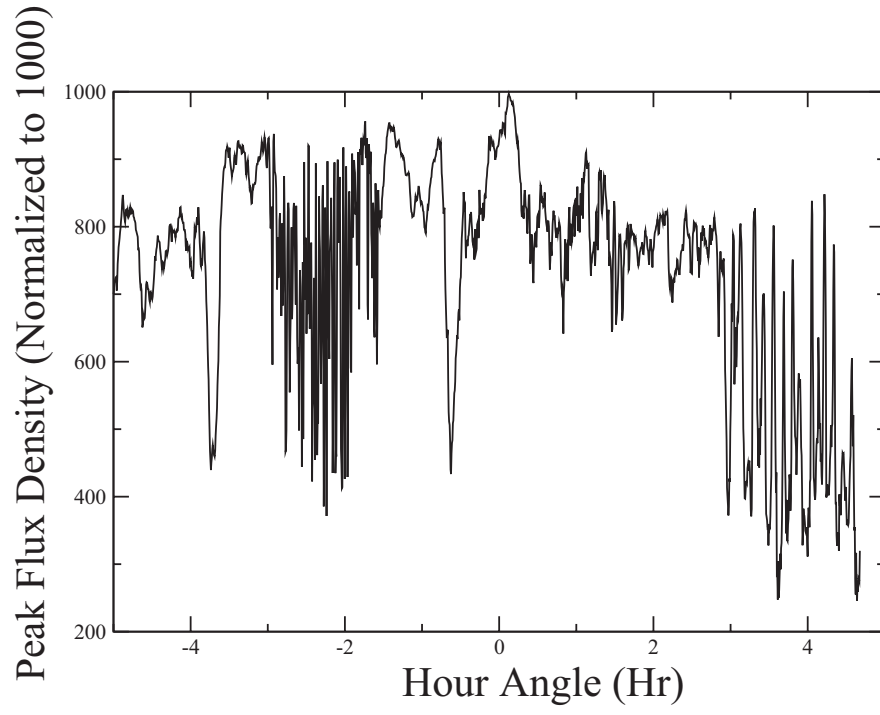
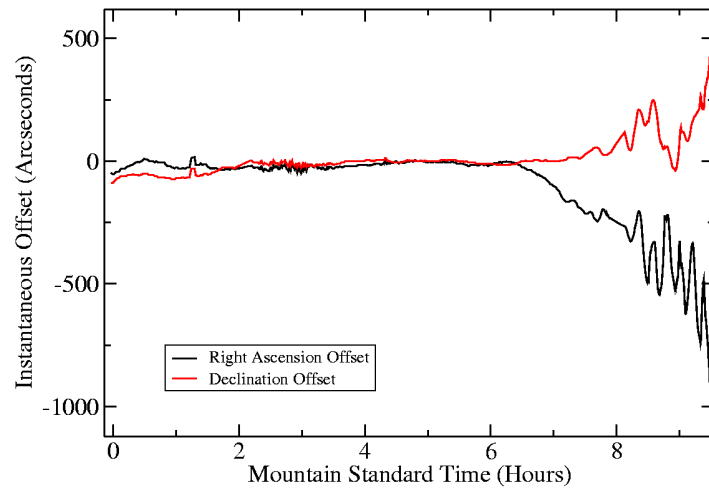


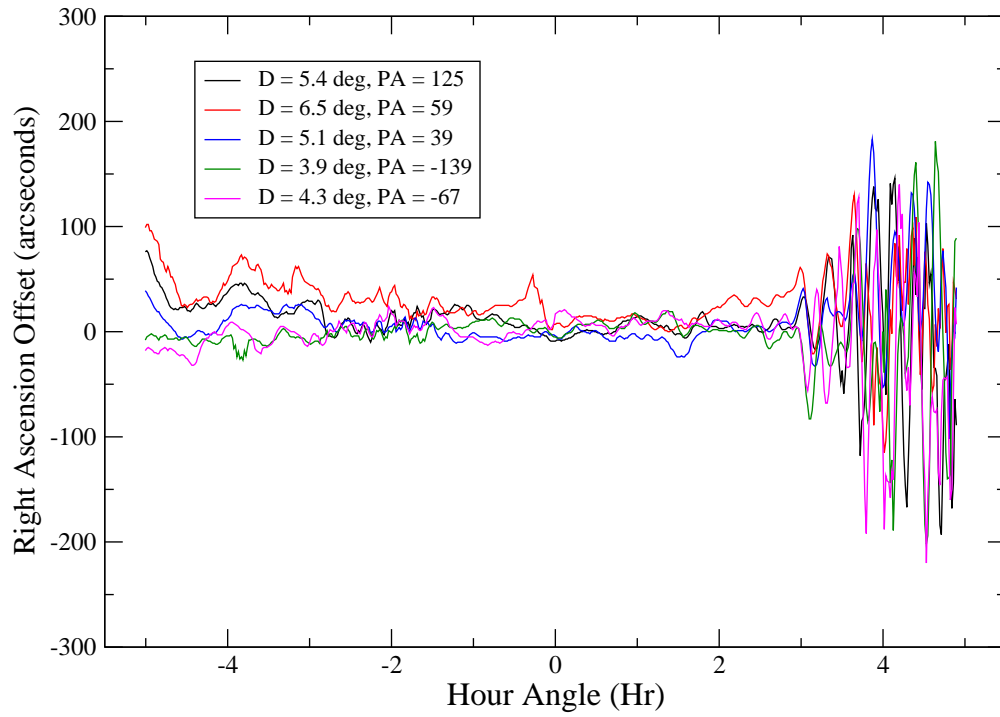
Fig. 14.— a) The phase of three antennas relative to a central antenna during an approximately 8 hr observations of Vir A illustrating many of the ionospheric phenomena typically observed at the VLA. All three antennas are located approximately 8 km from the reference antenna, but represent different azimuths. For the TID the observed parameters were a period of 750 s, phase slope of 50 deg km^{-1} , and a time lag of ~ 50 seconds over 20 km allowing Perley (2002) to derive a TID wavelength of 750 km and velocity of 200 m s^{-1} ; b) Same as in panel a except for two antennas at different distances along the same azimuth, indicating that to first order the phase effects of all the phenomena are proportional to baseline length; c) The instantaneous amplitude or apparent defocusing of Vir A over the same time scale as in panel a, (Hour Angle -4 corresponds to IAT Time ~ 8 hrs), sunrise occurred at $+3^{\text{h}}$; d) The refraction (or apparent position wander in both RA and Dec) of Virgo A over the same time scale as panel a; e,f) The apparent differential refraction in RA (e) and declination (f) as measured towards 5 objects located within 6 degrees of Vir A and of sufficient strength to be detected and tracked over the course of the observations. The time scale is the same as in panel c.





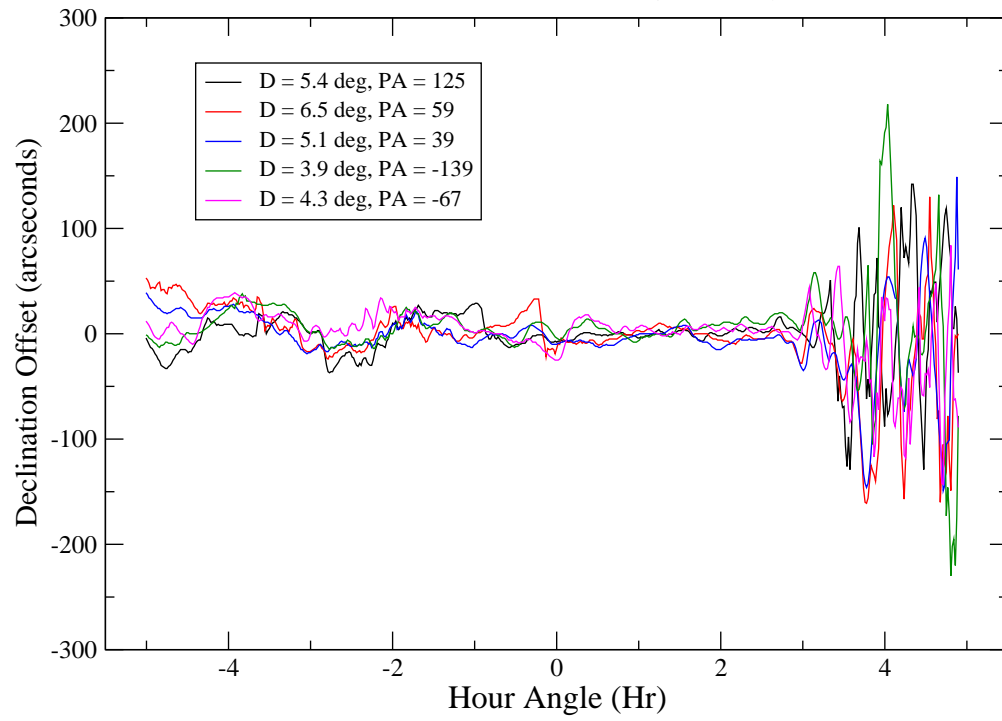


Differential Wander in Virgo A Field Right Ascension Shifts for Five Background Objects



Differential Wander in Virgo A Field

Declination Shifts for Five Background Objects



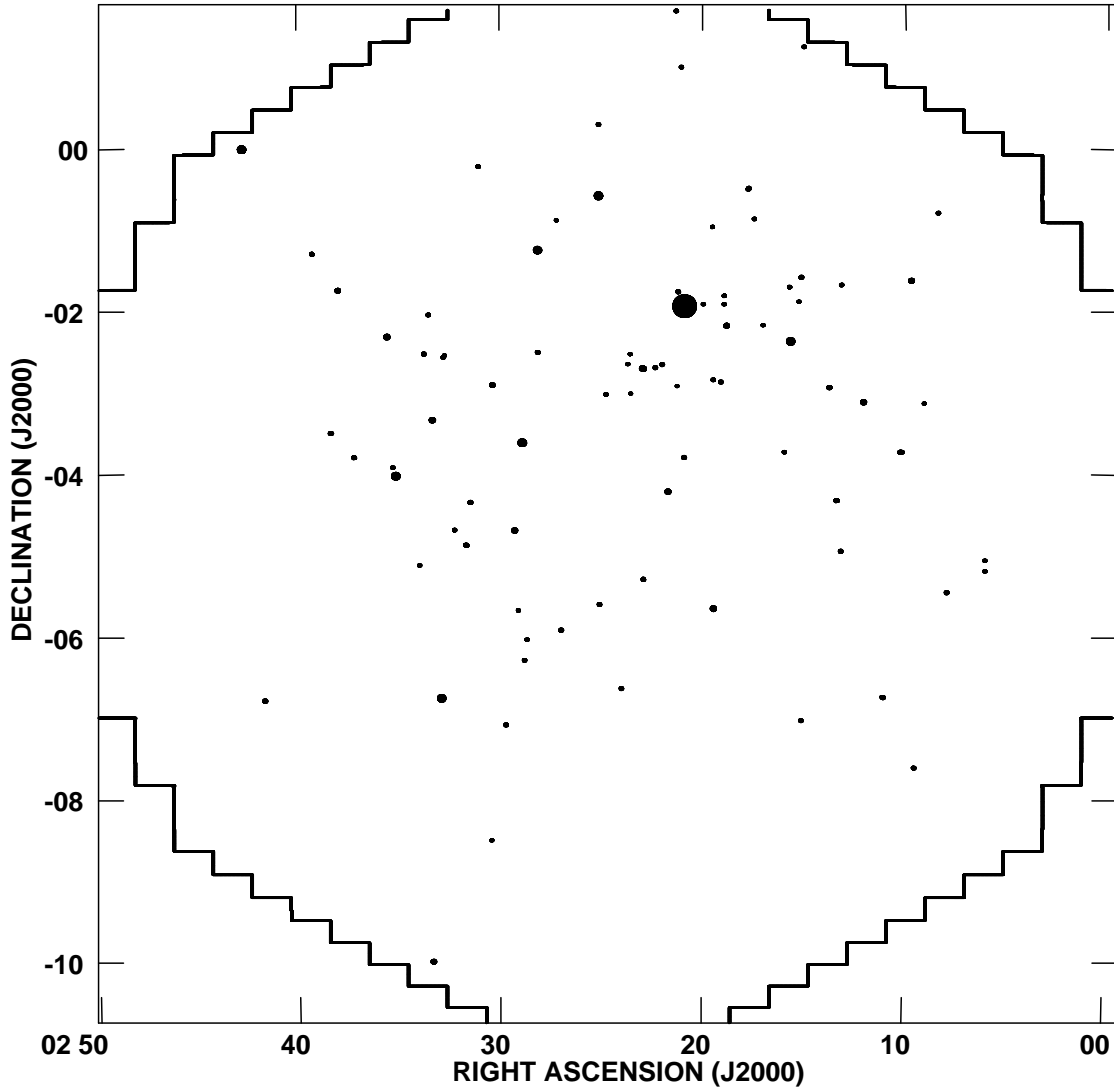


Fig. 15.— An example of the bias introduced by self-calibration. Symbols show the location of sources and are proportional to their flux densities. This field contains the (strong) source 3C 63 in the upper right. A clear non-uniform distribution of other sources across the field is evident, in addition to the decrease in number density expected from the primary beam attenuation. The jagged edges in the image indicate the boundaries of facets (§5); regions beyond the edges of the image have not been imaged.

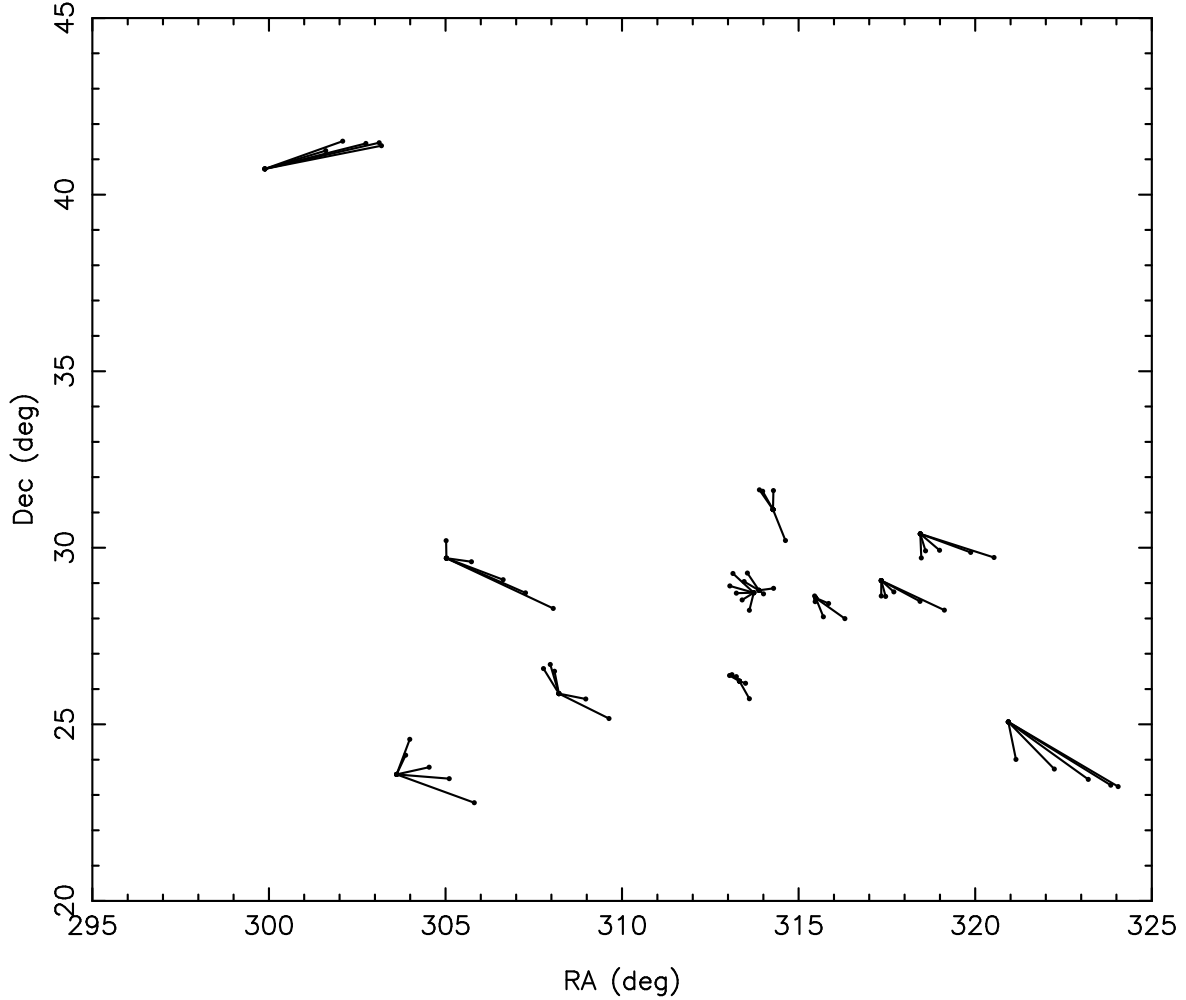


Fig. 16.— Differential, ionospheric-induced source wander within a field of view. The expected locations of various moderately strong sources within a single field of view is shown. The direction of each vector indicates direction of the position shift in five 5-min. intervals; the length of each vector is 100 times the actual displacement. Because the magnitude and direction of the wander is not the same for all sources, averaging over time results in sources being smeared out and apparently disappearing from view (viz. Figure 15).

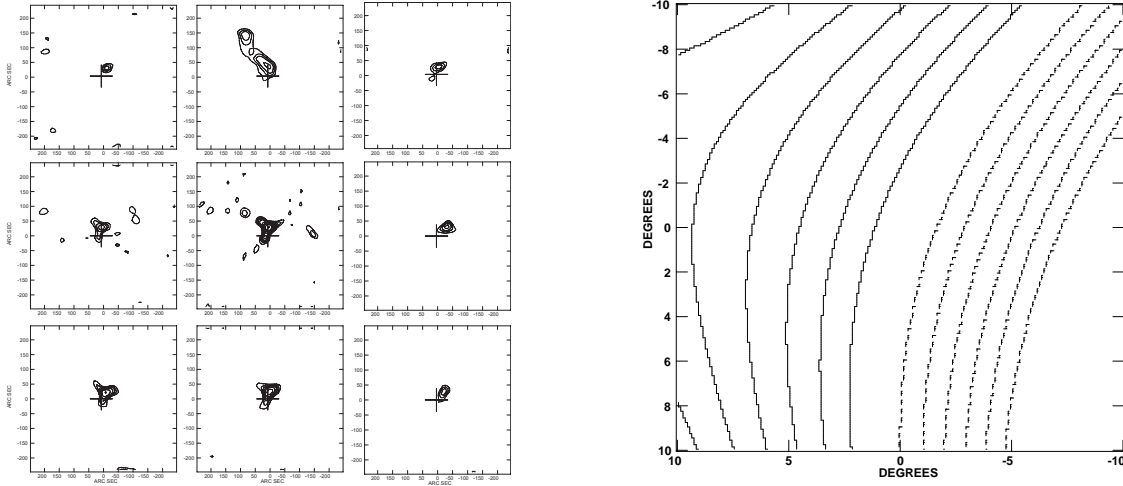


Fig. 17.— *Left*: A mosaic of NVSS sources assembled from a 1 min. snapshot of a full-field image at 74 MHz. The typical distance of each source from the phase center is 3° . The cross in each panel marks the nominal location of the NVSS source. Offsets from this nominal position are due to ionospheric refraction. *Right*: The Zernike model for $\phi_{\text{ion,lo}}$ over the VLA for the same time as the mosaic was constructed. See equation (6). Shown is the phase delay screen above one VLA antenna; because of the “small-array” approximation used, the phase delay screen over all other antennas is essentially the same. At a typical 350 km altitude, the phase delay screen shows structures on scales of roughly 100 km. Solid contours represent a phase advance, relative to a nominal phase, while dashed contours represent a phase delay. The most negative contour (lower right) represents a phase delay of -30° , and the most positive contour (upper left) represents a phase advance of $+30^\circ$.

Fig. 18.— The same field as in Figure 15, but calibrated by treating the ionosphere as a phase-delay screen. The distribution of sources across the field is far more uniform than before, though the primary beam attenuation near the edges of the image is still apparent. Abscissa: Right ascension; Ordinate: Declination. The jagged edges in the image indicate the boundaries of facets (§5); regions beyond the edges of the image have not been imaged. The black circle outside the field of view in the upper right is the location of an outlier field; this field contains a strong source outside the field of view that was also imaged.

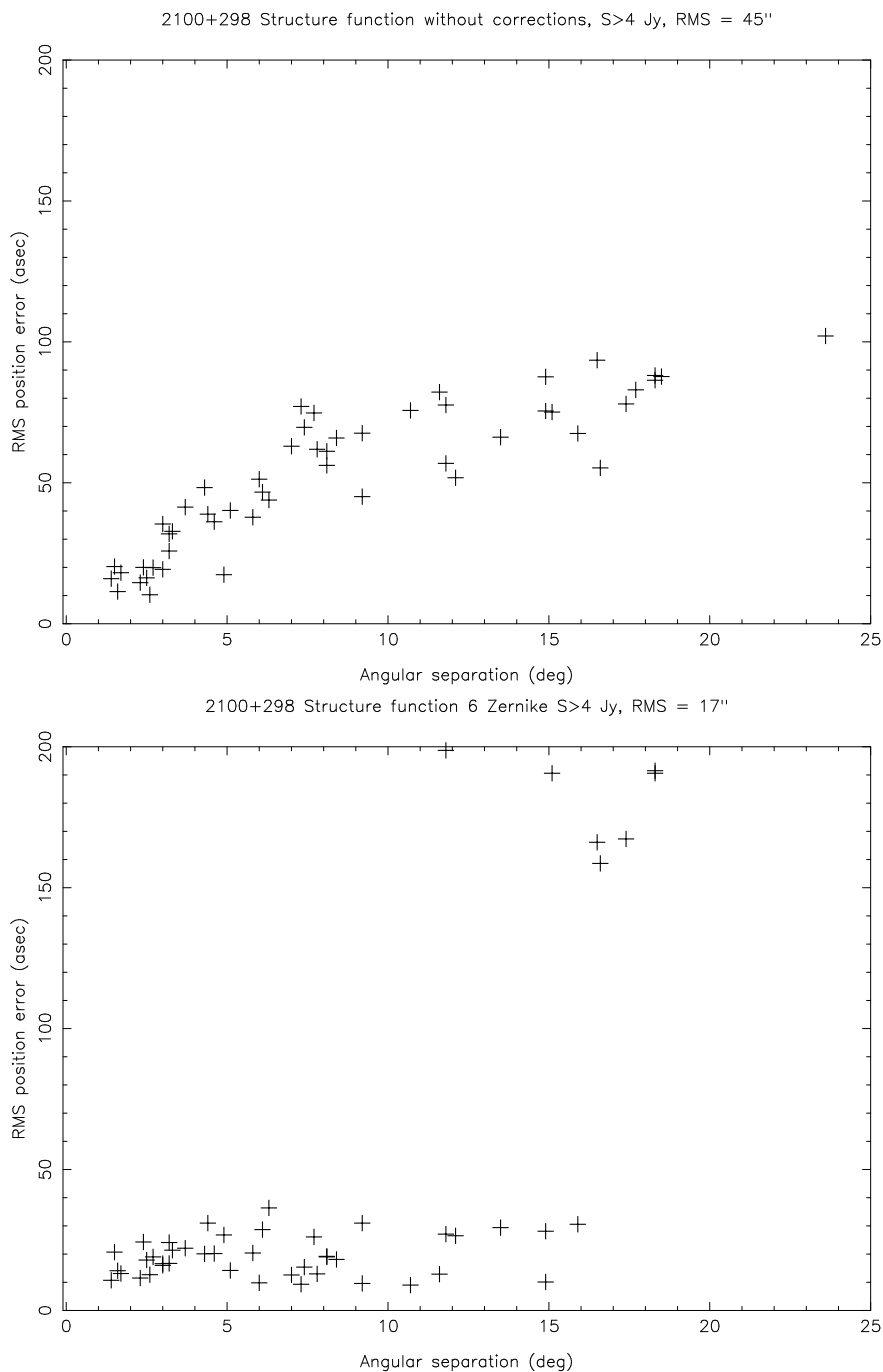


Fig. 19.— The rms jitter in apparent separations of pairs of sources with different separations made from a sequence of one minute snapshots taken over a period of several hours on a day with a moderately disturbed ionosphere. *Top* The rms jitter with no correction to the position difference. *Bottom* The rms jitter after applying an ionospheric model described by a 5-term Zernike phase screen determined from that snapshot. The large rms values at angular separations greater than approximately 15° result from Cyg A which was not corrected as part of this Zernike modeling.

Fig. 20.— Various (resolved) 3C sources at 74 MHz (left panel) and 330 MHz (right panel). For each source, we quote the rms noise level and the beam diameters in Table 7. All beams are circular unless otherwise noted. The contour levels are given in terms of the rms noise level in the image ($-3, 3, 6, 12, 24, 48, \dots$ times that rms noise level) and the beam is shown in the lower left. (a) 3C 10; (b) 3C 33; (c) The central strong sources of the Perseus cluster at 74 MHz. The source in the lower left is 3C 84, the compact source near the center is 3C 83.1A, and the extended radio galaxy in the upper right is NGC 1265; (d) 3C 84; (e) 3C 98; (f) 3C 129 (western source) and 3C 129.1 (eastern source); (g) 3C 144; (h) 3C 218; (i) 3C 219; (j) 3C 274 or Vir A; (k) 3C 327; (l) 3C 353; (m) 3C 390.3; (n) 3C 392; (o) 3C 405 or Cyg A; (p) 3C 445; (q) 3C 452; (r) 3C 461.

Fig. 21.— VLA + PT Link full synthesis 74 MHz image of Cas A, with a resolution of $\sim 8''$. The bottom bar shows the color transfer function in Jy. Image courtesy T. Delaney Delaney et al. (2004)

Table 1. Performance Characteristics of the VLA 74 MHz System

Center Frequency	73.8 MHz
Bandwidth	1.6 MHz
Primary Beamwidth (FWHM)	11°7
System Temperature (minimum)	1500 K
Aperture Efficiency	≈ 15%
Point Source Sensitivity (A or B configs., 8 hr)	25–50 mJy
Resolution (A configuration)	25''
(VLA + PT)	12''

Note. — See also Figures 6, 7, and 8.

Table 2. Comparison of VLA and Kühr et al. Flux Density Estimates

Name	Kühr et al. (Jy)	VLA (Jy)	Ratio	Remarks
3C 48	69.1	67.6 ± 0.4	0.978	Kühr et al. spectrum fit below observations
3C 98	98.9	98.0 ± 1.1	0.991	
3C 123	387.6	414.7 ± 1.3	1.070	Both Kühr et al. spectrum and VLA data look good
3C 147	67.1	55.3 ± 0.8	0.825	Kühr et al. estimate could be high, only one datum below 178 MHz and spectrum fit well below it
3C 219	96.6	94.8 ± 0.5	0.981	Kühr et al. spectrum looks good
3C 274	2281.3	2084.6 ± 1.3	0.914	Both Kühr et al. spectrum and VLA data look good
3C 327	93.1	118.4 ± 0.8	1.272	Kühr et al. spectrum could be low, falls below 38 MHz datum but fits 80 MHz datum
3C 353	437.0	443.8 ± 0.8	1.016	Kühr et al. spectrum is unreliable below 160 MHz
3C 390.3	107.2	97.1 ± 0.4	0.906	Kühr et al. spectrum may be high, misses 38 MHz datum
3C 445	62.6	49.2 ± 0.3	0.785	VLA flux density unestimated?; B-configuration data only
3C 452	142.5	142.6 ± 0.2	1.001	

Note. — The uncertainties given for the VLA measurements are merely the formal standard deviations from fits to the images. Little significance should be attached to them.

Table 3. Zernike Polynomials $Z_n^l(\rho, \phi)$

n	l			
	0	1	2	3
1	...	$\rho e^{i\phi}$
2	$2\rho^2 - 1$...	$\rho^2 e^{2i\phi}$...
3	...	$(3\rho^3 - 2\rho)e^{i\phi}$...	$\rho^3 e^{3i\phi}$

Note. — The polynomials are expressed in terms of a radial distance from the phase center ρ and a position angle ϕ . The Z_0^0 polynomial is not used because it represents a total phase contribution (“piston”) to which the interferometer is insensitive.

Table 4. Evolving Techniques for Ionospheric Calibration

Method	Parameterization	Imaging Capability	FoV	Baseline	Reference
Simple geometric shift	None re-register position of known sources	No restrictions	Full field ($\lambda/D_{station}$)	≤ 5 km	Erickson (1984)
Classical Self Calibration	$\phi_i(t)$ - one term per i station	Bright, isolated sources (e.g. 3C objects)	$\leq 15'$	≤ 400 km	Kassim et al. (1993) Gizani et al. (2005) Lazio et al. (2006)
Field-based calibration	$\phi(t, \alpha, \delta)$ - single term for entire array	No restrictions (used for VLSS)	Full field ($\lambda/D_{station}$)	≤ 12 km	Cotton et al. (2004)
Joint Multi-source Self-calibration	$\phi(t, \alpha, \delta)$ - one term per i stations	No restrictions	Full field ($\lambda/D_{station}$)	≤ 400 km	TBD

Table 5. 74 MHz VLA Classical Confusion Limits

Configuration	Resolution (")	Confusion Level (mJy)
A	25	7
B	77	40
C	240	250
D	744	1500

Table 6. 74 MHz VLA Polyhedral Imaging

Configuration	θ_{facet} (')	N_{facet}
A	13	720
B	22	250
C	39	80
D	69	25

Table 7. 74 MHz and 330 MHz Observations of Sources

Source	Alternative Name	Integration Time			74 MHz		330 MHz	
		A-conf. (min)	B-conf. (min)	C-conf. (min)	beam ('')	rms (Jy)	beam ('')	rms (mJy)
3C010	Tycho SNR	71	80	35	80	0.36	7.9×6.7	2.0
3C033		41	62	29	25	0.14	7.0	7.4
Perseus Cluster		51	73	111	94	0.16	20.0	6.7
3C084	NGC1275	51	73	111	25	0.08	6.0	2.6
3C098		44	53	36	25	0.13	8.0	3.9
3C129		13	93	87	83×75	0.10	65.0	6.5
3C144	M1, Crab SNR	92	14	19	25	0.12	18.0	47.4
3C218	Hydra A	16	16	18	30	0.17	10.0	26.0
3C219		82	82	58	25	0.06	6.0	1.9
3C274	M87, Virgo A	71	71	49	25	0.08	23.0	13.8
3C327		52	51	21	25	0.38	6.0	4.3
3C353		51	51	27	25	0.16	7.5	7.3
3C390.3		72	81	27	29×25	0.05	7.5	2.4
3C392	W44, SNR G34.7-0.4	51	51	27	300	1.10	25.0×22	15.6
3C405	Cyg A	9	9	10	31×26	4.63	5.0	53.0
3C445		31	42	...	30	0.03	10.4×9.0	3.0
3C452		76	82	33	25	0.12	7.0	2.8
3C461	Cas A	7	9	7	30	17.0	18.0	227.0

Table 8. Peak Intensities and Flux Densities of 3C Sources at 74 MHz

Name	I (Jy beam ⁻¹)	S (Jy)
3C 10	13.0	252.1 ± 1.94
3C 33	55.3	105.3 ± 0.41
3C 48	66.9	67.6 ± 0.44
3C 84	82.2	171.3 ± 0.52
3C 98	35.7	98.0 ± 1.12
3C 123	387.8	414.7 ± 1.31
3C 129	27.8	70.4 ± 0.48
3C 144	305.6	1811.3 ± 3.07
3C 147	57.2	55.3 ± 0.82
3C 161	85.6	87.5 ± 0.39
3C 196	133.1	129.8 ± 0.95
3C 218	270.2	644.2 ± 1.83
3C 219	38.9	94.8 ± 0.50
3C 273	142.2	140.6 ± 1.42
3C 274	567.2	2084.6 ± 1.29
3C 286	27.6	27.2 ± 0.76
3C 295	111.6	107.9 ± 1.62
3C 298	95.3	92.4 ± 1.22
3C 327	52.8	118.4 ± 0.77
3C 353	152.2	443.8 ± 0.76
3C 380	124.4	143.7 ± 2.57
3C 390.3	45.4	97.1 ± 0.42
3C 392	9.2	715.7 ± 2.88
3C 405	9308.3	17205.0 ± 1.44
3C 445	9.2	49.2 ± 0.32

Table 8—Continued

Name	I (Jy beam ⁻¹)	S (Jy)
3C 452	38.1	142.6 ± 0.19
3C 461	2362.2	17693.9 ± 12.12
3C 468.1	42.0	40.7 ± 0.66

This figure "f3.jpg" is available in "jpg" format from:

<http://arxiv.org/ps/0704.3088v1>

This figure "f4.jpg" is available in "jpg" format from:

<http://arxiv.org/ps/0704.3088v1>

This figure "f6a.jpg" is available in "jpg" format from:

<http://arxiv.org/ps/0704.3088v1>

This figure "f6b.jpg" is available in "jpg" format from:

<http://arxiv.org/ps/0704.3088v1>

This figure "f9.jpg" is available in "jpg" format from:

<http://arxiv.org/ps/0704.3088v1>

This figure "f11.jpg" is available in "jpg" format from:

<http://arxiv.org/ps/0704.3088v1>

This figure "f12.jpg" is available in "jpg" format from:

<http://arxiv.org/ps/0704.3088v1>

This figure "f13.jpg" is available in "jpg" format from:

<http://arxiv.org/ps/0704.3088v1>

This figure "f18.jpg" is available in "jpg" format from:

<http://arxiv.org/ps/0704.3088v1>

This figure "f20a.jpg" is available in "jpg" format from:

<http://arxiv.org/ps/0704.3088v1>

This figure "f20aa.jpg" is available in "jpg" format from:

<http://arxiv.org/ps/0704.3088v1>

This figure "f20ab.jpg" is available in "jpg" format from:

<http://arxiv.org/ps/0704.3088v1>

This figure "f20ac.jpg" is available in "jpg" format from:

<http://arxiv.org/ps/0704.3088v1>

This figure "f20ad.jpg" is available in "jpg" format from:

<http://arxiv.org/ps/0704.3088v1>

This figure "f20ae.jpg" is available in "jpg" format from:

<http://arxiv.org/ps/0704.3088v1>

This figure "f20af.jpg" is available in "jpg" format from:

<http://arxiv.org/ps/0704.3088v1>

This figure "f20ag.jpg" is available in "jpg" format from:

<http://arxiv.org/ps/0704.3088v1>

This figure "f20ah.jpg" is available in "jpg" format from:

<http://arxiv.org/ps/0704.3088v1>

This figure "f20ai.jpg" is available in "jpg" format from:

<http://arxiv.org/ps/0704.3088v1>

This figure "f20aj.jpg" is available in "jpg" format from:

<http://arxiv.org/ps/0704.3088v1>

This figure "f20b.jpg" is available in "jpg" format from:

<http://arxiv.org/ps/0704.3088v1>

This figure "f20c.jpg" is available in "jpg" format from:

<http://arxiv.org/ps/0704.3088v1>

This figure "f20d.jpg" is available in "jpg" format from:

<http://arxiv.org/ps/0704.3088v1>

This figure "f20e.jpg" is available in "jpg" format from:

<http://arxiv.org/ps/0704.3088v1>

This figure "f20f.jpg" is available in "jpg" format from:

<http://arxiv.org/ps/0704.3088v1>

This figure "f20g.jpg" is available in "jpg" format from:

<http://arxiv.org/ps/0704.3088v1>

This figure "f20h.jpg" is available in "jpg" format from:

<http://arxiv.org/ps/0704.3088v1>

This figure "f20i.jpg" is available in "jpg" format from:

<http://arxiv.org/ps/0704.3088v1>

This figure "f20j.jpg" is available in "jpg" format from:

<http://arxiv.org/ps/0704.3088v1>

This figure "f20k.jpg" is available in "jpg" format from:

<http://arxiv.org/ps/0704.3088v1>

This figure "f201.jpg" is available in "jpg" format from:

<http://arxiv.org/ps/0704.3088v1>

This figure "f20m.jpg" is available in "jpg" format from:

<http://arxiv.org/ps/0704.3088v1>

This figure "f20n.jpg" is available in "jpg" format from:

<http://arxiv.org/ps/0704.3088v1>

This figure "f20o.jpg" is available in "jpg" format from:

<http://arxiv.org/ps/0704.3088v1>

This figure "f20p.jpg" is available in "jpg" format from:

<http://arxiv.org/ps/0704.3088v1>

This figure "f20q.jpg" is available in "jpg" format from:

<http://arxiv.org/ps/0704.3088v1>

This figure "f20r.jpg" is available in "jpg" format from:

<http://arxiv.org/ps/0704.3088v1>

This figure "f20s.jpg" is available in "jpg" format from:

<http://arxiv.org/ps/0704.3088v1>

This figure "f20t.jpg" is available in "jpg" format from:

<http://arxiv.org/ps/0704.3088v1>

This figure "f20u.jpg" is available in "jpg" format from:

<http://arxiv.org/ps/0704.3088v1>

This figure "f20v.jpg" is available in "jpg" format from:

<http://arxiv.org/ps/0704.3088v1>

This figure "f20w.jpg" is available in "jpg" format from:

<http://arxiv.org/ps/0704.3088v1>

This figure "f20x.jpg" is available in "jpg" format from:

<http://arxiv.org/ps/0704.3088v1>

This figure "f20y.jpg" is available in "jpg" format from:

<http://arxiv.org/ps/0704.3088v1>

This figure "f20z.jpg" is available in "jpg" format from:

<http://arxiv.org/ps/0704.3088v1>

This figure "f21.jpg" is available in "jpg" format from:

<http://arxiv.org/ps/0704.3088v1>